Journal of Multiscale Modelling (World Scientific)

ISSN (print): 1756-9737 | ISSN (online): 1756-9745

Impact factor = 1.5

Accepted July 20th 2023

CROSS DIFFUSION AND HIGHER ORDER CHEMICAL REACTION EFFECTS ON HYDROMAGNETIC COPPER-WATER NANOFLUID FLOW OVER A ROTATING CONE WITH POROUS MEDIUM

Padmaja K[1], B Rushi Kumar[1]*, O. Anwar Bég[2] and Tasveer A. Bég[3]

[1]*Department of Mathematics, Vellore Institute of Technology, Vellore, 632014, Tamilnadu,* ***India****.*
[2]*Professor and Director-Multi-Physical Engineering Sciences Group, Corrosion Lab, 3-08, Mechanical Engineering Department, University of Salford, Manchester, M54WT,* ***UK.***

[3]*Engineering Mechanics Research, Israfil House, Dickenson Rd., Manchester, M13,* ***UK.***

**Corresponding author. E-mail(s): rushikumar@vit.ac.in*

Contributing authors: padmaja.k@vit.ac.in; O.A.Beg@salford.ac.uk; tasveerabeg@gmail.com

ABSTRACT

Spin coating of engineering components with advanced functional nanomaterials which respond to magnetic fields is growing. Motivated by exploring the fluid dynamics of such processes, a mathematical model is developed for chemically reactive $Cu-H_2O$ magnetohydrodynamic (MHD) nanofluid swirl coating flow on a revolving vertical electrically insulated cone adjacent to a porous medium under a radial static magnetic field. Heat and mass transfer is included and Dufour and Soret cross diffusion effects are also incorporated in the model. Thermal and solutal buoyancy forces are additionally included. The Tiwari-Das nanoscale model has been used. To simulate chemical reaction of the diffusing species encountered in manufacturing processes, a higher order chemical reaction formulation is also featured. Via suitable scaling transformations, the governing nonlinear coupled partial differential conservation equations and associated boundary conditions are reformulated as a nonlinear ordinary differential boundary value problem. MATLAB-based shooting quadrature with a Runge-Kutta method is deployed to solve the emerging system. Concentration, temperature, velocity variations for various non-dimensional flow parameters have been visualized and analysed. In addition, key wall characteristics i. e. radial and circumferential skin friction, Nusselt number, Sherwood number have also been computed. Validation with earlier studies is also included. The simulations indicate that when compared to a lower order chemical reaction, a higher order chemical reaction allows a greater rate of heat and mass transfer at the cone surface. Increasing Dufour (diffuso-thermal) and Soret number generally reduce radial and circumferential skin friction and also Nusselt number whereas they elevate Sherwood number. Both skin friction components are also suppressed with increasing Richardson number. Strong deceleration in the tangential and circumferential velocity components is induced with greater magnetic field.

KEYWORDS: *Higher order chemical reaction, Porous medium, magnetic nanofluid, swirl nano-coating manufacturing; vertical cone; Dufour and Soret effects; Sherwood number.*

1 INTRODUCTION

In numerous manufacturing process systems, chemical reactions arise. These include reaction-bonding of ceramics, chemical vapour deposition in diamond coating, direct laser melting processes for fuel cell bipolar plate fabrication, reaction injection moulding, electro-chemical machining, photopolymerization and magnetohydrodynamic spin coating with electroconductive functional materials [1-5]. Mathematical models of the multi-physico-chemical transport phenomena inherent to such processes are very beneficial in optimizing designs. The order of a chemical reaction explains the relationship between the concentration of a species and the rate at which the reaction takes place. There is a wide range of applications for heat and mass transfer in porous media in particular with higher order chemical reactions including filtration, distillation, cooling, drying and coating deposition. Many of the reactions that take place in these systems cannot be simulated with a first order homogenous destructive model. N^{th} order models are required in which chemical reaction rate is proportional to the n^{th} power of species' concentration. Chemical reactions occur at a faster rate as the reaction order increases which in turn influences the heat, mass and momentum characteristics and this effectively modifies the final constitution of engineered products. Higher order chemical reaction influence in porous media and purely fluent media have previously been investigated by a number of researchers. Rahman and Al-Lawatia [6] studied the influence of higher order chemical reaction on micropolar convection from a nonlinear stretching sheet in a Darcian porous medium. They showed that wall mass transfer rate is reduced with greater Darcy parameter and is also strongly influenced by higher order reaction and wall concentration parameter. Palani *et al.* [7] computed the time-dependent hydromagnetic viscoelastic flow from a stretching surface in the presence of higher order chemical reaction. They noted that species (concentration) boundary layer thickness is greatly increased for a third order chemical reaction as compared to either first or second-order chemical reactions. Sastry [8] used MATLAB bvp4c quadrature to simulate the phase change in mixed convective dissipative flow from a vertical surface adjacent to a non-Darcian porous medium with higher order chemical reaction. He showed that increasing order of chemical reaction reduces velocity and increases momentum boundary layer thickness whereas it enhances concentration and species boundary layer thickness. He also observed that melting (phase change) accelerates the flow but reduces thermal boundary layer thickness.

With the increasing demand for the manufacturing more sustainable products, heat transfer using fluids must be efficient with minimal energy losses. To transport heat more effectively,

conventional liquids such as polymers, gels and water can be mixed with metals that have a high thermal conductivity. This is particularly critical in coating operations since the wall heat transfer (and mass transfer) rates can be manipulated via thermal conductivity and viscosity to achieve more robust designs. Choi and Eastman [9] developed nanofluids as colloidal suspensions of nanometer-sized particles engineered into a base fluid (liquid solvent), in order to achieve overall elevation in thermal performance. Nanoparticles may be caron-based e.g. silicon carbide or metallic/metallic oxides e.g. copper, titaniu, molybdenum, aluminium oxide, silver oxide etc. Further advantages offered by nano-based materials are enhanced chemical resistance, erosion and abrasion resistance, agglomeration reduction, resistance to UV light, anti-fouling, durability and anti-bacterial (sterilization) properties [10]. Nano-coatings are defined as coatings which feature any nano-material component e. g. nanotubes, nanofillers, nanoparticles, nanowires etc. A further key characteristic of nanoparticles embedded in liquid coatings is the considerable surface area: volume ratio which achieves enhanced surface activity, improved interactions and allows optimized protection with lower concentrations. In parallel with laboratory-based studies of nanofluids, a variety of mathematical models have been developed to simulate nanoscale characteristics, from a continuum view-point. The most popular are the Buongiorno two-component model [11] (which emphasizes thermophoretic body force and Brownian motion dynamics) and the Tiwari-Das volume fraction model [12]. The latter has the advantage that actual nanoparticle materials can be simulated via the use of specific relations for thermal conductivity, heat capacity, density, viscosity etc. Copper nanoparticles in particular have the advantage of very high thermal conductivity, excellent anti-corrosion ability and proven anti-bacterial properties which make them ideal for biomedical coating operations [13]. Other popular combinations are cobalt and iron [14]. Both Buongiorno and Tiwari-Das models have been deployed extensively in recent years for simulating nano-coating manufacturing flows where chemical reactions are also considered. These studies have also featured an extensive range of numerical methods which are required to solve the nonlinear boundary value problems that arise in such flows. Shamshuddin *et al.* [15] used the Adomian decomposition method (ADM) to compute the non-Newtonian (Sisko) nanofluid from a bi-directional stretching sheet in a porous medium, with radiative flux, homogeneous–heterogeneous chemical reactions and convective wall heating. They noted that greater homogenous chemical reaction parameter values weakly suppress concentration whereas higher heterogeneous reaction strongly depletes it (and also species boundary layer thickness). Swain *et al.* [16] used the Buongiorno model to study the hydromagnetic nanofluid stretching sheet coating flow with radiative flux and higher order chemical reaction. They observed that

stronger magnetic field and mass transfer parameter boosts the skin friction coefficient and mass flux at the wall whereas it suppresses heat flux to the wall. They also showed that with higher order chemical reaction and Prandtl number, both heat flux and mass flux to the wall are suppressed. Eid *et al.* [17] examined the 3-dimensional laminar boundary layer flow of a Prandtl nanofluid flow over a convectively heated sheet in a permeable medium with nonlinear radiation and high-order chemical reaction. They noted that Sherwood number (mass transfer rate to the wall) diminishes with greater order of the chemical reaction whereas both velocity and temperature fields are assisted. Pattnaik *et al.* [18] used MATLAB bvp5c quadrature and Adams-Moulton predictor–corrector numerical schemes with the Tiwari-Das model to simulate the catalytic reactive species diffusion in axisymmetric coating enrobing forced convection boundary layer magnetic titanium dioxide-water nanofluid flow from an axially stretching horizontal cylinder in Darcy-Forchheimer porous media. They considered dual chemical reacting species and showed that different mass transfer rates are induced with a variety of chemical reactions. They further showed that increasing Darcian parameter depletes local Nusselt number magnitudes at the cylinder surface whereas greater volume fraction of titanium oxide nanoparticles enhances temperatures significantly.

The above studies did not consider rotation of the substrate i. e. the body being coated was not rotating. The use of a *rotating cone* features in a variety of coating and other processes in manufacturing engineering including spin deposition of ferromagnetic nanocoatings [19], electrodeposition of copper from an acid electrolyte via limiting current mass transport techniques [20], high quality finishing of aerospace components [21], polymer synthesis [22] and sublimation processes from naphthalene-coated rotating conical configurations [23]. The rotation of the cone invokes centrifugal body forces which strongly manipulate the heat, mass and momentum characteristics. Inspired by these applications, a number of investigations of hydromagnetic rotating cone viscous flows have been communicated. Roy *et al*. [24] examined the transient magnetohydrodynamic flow from a rotating cone in a rotating Newtonian fluid using a finite difference method. They showed that tangential and azimuthal directions skin friction coefficients increase when the angular velocity of the fluid or body increases with time. They also found that for the case where the angular velocity of the fluid exceeds that of the body, the velocity profiles attain asymptotic values at the free stream in an oscillatory manner, whereas increasing magnetic field or cone surface suction reduces these oscillations. Bég *et al.* [25] used the Keller-box finite difference method to simulate natural convection magnetohydrodynamic flow from a spinning vertical cone to an anisotropic Darcian porous

medium They showed that tangential and azimuthal (swirl) velocity are boosted with increasing permeability whereas temperatures are depressed. They also observed that stronger magnetic field damps the tangential velocity field and Nusselt number at the cone surface but boosts thermal boundary layer thickness. Several articles addressing rotating cone magnetic nanofluid dynamics have also been presented in recent years. Ahmed *et al.* [26] used the Blottner finite difference method to numerically evaluate the swirling flow of magnetized Ellis rheological nanofluids doped with micro-organisms from a rotating cone with Ohmic dissipation and heat generation. They showed that Nusselt and Sherwood numbers are accentuated with increasing rotation parameter whereas velocity and temperature gradients are suppressed with increasing bioconvection Rayleigh number and magnetic parameter. Zohra *et al.* [27] used MATLAB software and the Tiwari-Das model to compute the steady laminar natural convective anisotropic slip boundary layer flows from a rotating vertical cone embedded in ethylene glycol bionanofluid with Stefan wall blowing effects. They considered four different non-particles i.e. Copper (Cu), Alumina (Al_2O_3), Copper Oxide (Cuo), Titanium Oxide (TiO_2). They showed that skin friction factor is elevated with tangential slip, magnetic field and Schmidt number whereas it is strongly depleted with stronger blowing parameter and spin parameters. Additionally, they showed that maximum skin friction and Nusselt number heat transfer rates are attained for copper nanoparticles whereas they are minimal for TiO_2nanoparticles. Further studies of rotating magnetic nanofluid flows have been communicated by Rana *et al.* [28] (for time-dependent revolving stretching sheets in nanocoating fabrication), Moatimid *et al.* [29] (for viscoplastic nanofluids in the conical gap zone) and Abdal *et al.* [30] (for non-Fourier Sutterby polymeric nanofluid slip transport from a rotating cone). All these analyses have confirmed the profound influence of rotational body force on transport characteristics in magnetized nanofluid coating systems.

In the present study, motivated by swirl coating with magnetic nanofluids, a mathematical model is developed for *laminar steady-state chemically reactive $Cu-H_2O$ magnetohydrodynamic (MHD) nanofluid swirl coating flow from a rotating vertical electrically insulated cone adjacent to a porous medium under a radial static magnetic field*. Higher order chemical reactions have been studied in the context of magnetic nanofluids by Jagadha *et al.* [31], Alaidrous and Eid [32], Gopal *et al.* [33] and Rajani and Hemalatha [34]. However, these *studies neglected body rotation effects and furthermore did not include Dufour and Soret cross diffusion effects*. Thermo-diffusion and diffuso-thermal effects are important in mass transfer coating operations. The Soret effect is associated with mass flux phenomena

induced by heat diffusion, whereas the Dufour effect is related to the energy flux generated by the concentration (solute) difference. Both effects have been shown to have a significant influence on magnetic nanofluid coating flows in a range of studies including Bhatti *et al.* [35] (who considered magnetic Fe_3O_4-water-based nanofluids), Sulochana *et al.* [36] (who examined magnetic titanium oxide nanofluids) and Siddique *et al.* [37] (who considered viscoelastic magnetic nanofluids). All these studies identified that Dufour and Soret effects modify the heat and mass diffusion rates substantially. In the present simulations, therefore the novelties are the *simultaneous consideration of cross diffusion, cone rotation and furthermore thermal and solutal buoyancy forces are additionally incorporated for the case of* $Cu - H_2O$ *nanofluid*. To simulate chemical reaction of the diffusing species encountered in manufacturing processes, a higher order chemical reaction formulation is also featured. The Tiwari-Das model is deployed and a Darcian formulation utilized for porous media drag effects. Using appropriate similarity variables, the governing nonlinear coupled partial differential conservation equations and associated boundary conditions are reformulated as a nonlinear ordinary differential boundary value problem. MATLAB-based shooting quadrature with a Runge-Kutta method is deployed to solve the emerging system. Concentration, temperature, velocity variations for various non-dimensional flow parameters have been visualized and analysed. In addition, key wall characteristics i. e. radial and circumferential skin friction, Nusselt number, Sherwood number have also been computed. Validation with earlier studies is also included. Copper nanoparticles (Cu) are examined in this study as they offer excellent anti-viral properties in biomedical coatings [38-41]. The breakdown of the paper is as follows: The mathematical boundary layer swirl hydromagnetic nano-coating model with nanoscale properties is developed in section 2. In section 3, the nonlinear equations that govern the system are solved numerically with MATLAB bvp4c quadrature and the Runge-Kutta shooting method. Validation with earlier studies is included [42]. In section 4, extensive graphical illustrations for all thermofluid characteristics are presented in addition to tables. Detailed interpretation of all the numerical results is provided. Section 5 lists the principal conclusions of the present investigation with some suggested future pathways for extending the analysis.

2 MATHEMATICAL MODEL

Consider the laminar, incompressible, steady-state swirling magnetohydrodynamic coating boundary layer flow of copper-water nanofluid from a rotating vertical cone with a vertex angle α, radius r and slant height *L* as shown in **Figure 1**. An (*x*,*y*,*z*) coordinate system is adopted. The velocity components in these directions are *u*,*v*,*w*, respectively.

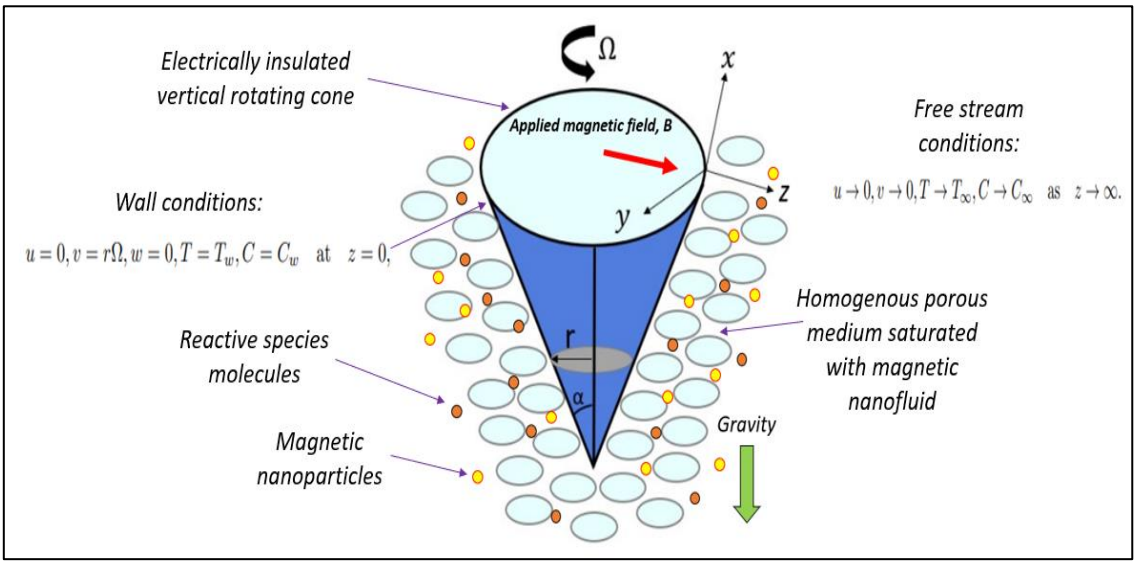

Fig. 1 Geometry of cone magnetic nanofluid spin coating process

The cone is engulfed in a porous medium (filtration regime) saturated with the nanofluid and containing a reactive species. The cone spins with a constant rotational velocity, Ω. Relative to the ambient conditions, the cone wall temperature and species concentration are taken to be higher. An n^{th} order chemical reaction is considered. Dufour and Soret effects are present. The imbalance in the temperatures and species concentrations generates thermal and solutal buoyancy forces (natural convection). The magnetic Reynolds number is sufficiently small to neglect the induced magnetic field in comparison to the applied magnetic field, B_o which acts in the circumferential direction (*z*). Since there is no applied or polarisation voltage imposed on the flow field, the electrical field vanishes, and the cone surface is electrically insulated. Ohmic and viscous dissipation and Maxwell displacement current effects are neglected. The boundary layer equations governing the flow (mass, momentum, energy and species conservation) may be presented as follows:

$$\frac{\partial u}{\partial x}+\frac{\partial w}{\partial z}+\frac{u}{x}=0, \tag{1}$$

$$\begin{aligned}\rho_{nf}(u\frac{\partial u}{\partial x}+w\frac{\partial u}{\partial z}+\frac{u^2}{x})=\mu_{nf}(\frac{\partial^2 u}{\partial z^2})-\frac{\mu_{nf}}{K^*}u-\sigma_{nf}B_o^2u \\ +(\rho\beta)_{nf}g(T-T_\infty)cos\alpha+(\rho\beta)_{nf}g(C-C_\infty)cos\alpha,\end{aligned} \tag{2}$$

$$\rho_{nf}(u\frac{\partial v}{\partial x}+w\frac{\partial v}{\partial z}+\frac{uv}{x})=\mu_{nf}(\frac{\partial^2 v}{\partial z^2})-\frac{\mu_{nf}}{K^*}v-\sigma_{nf}B_o^2v, \tag{3}$$

$$u\frac{\partial T}{\partial x}+w\frac{\partial T}{\partial z}=\frac{\kappa_{nf}}{(\rho C_p)_{nf}}\frac{\partial^2 T}{\partial z^2}+\frac{D_mK_T}{C_sC_p}\frac{\partial^2 C}{\partial z^2}, \tag{4}$$

$$u\frac{\partial C}{\partial x}+w\frac{\partial C}{\partial z}=D_m\frac{\partial^2 C}{\partial z^2}+\frac{D_mK_T}{T_m}\frac{\partial^2 T}{\partial z^2}-k_r(C-C_\infty)^n. \tag{5}$$

The prescribed wall (cone surface) and free stream boundary conditions, take the form:

$$\begin{aligned}u=0,v=r\Omega,w=0,T=T_w,C=C_w \quad \text{at} \quad z=0,\\ u\to 0,v\to 0,T\to T_\infty,C\to C_\infty \quad \text{as} \quad z\to\infty.\end{aligned} \tag{6}$$

Here *C is the species concentration; C_p-specific heat at constant pressure; C_s-concentration susceptibility; C_w - nanoparticle concentration at wall; C_∞-nanoparticle concentration in free stream; D_m-molecular diffusivity; g-gravitational acceleration; K_T -thermal diffusivity ratio; k_r-chemical reaction rate; $K*$ -permeability of porous medium; n-an integer which denotes order of the chemical reaction; r-cone radius; T-nanofluid temperature; T_w-nanofluid wall temperature; T_∞-nanofluid temperature in free stream; T_m-mean fluid temperature; σ_{nf} - nanofluid electrical conductivity*. Thermophysical properties of the dilute nanofluid are given by [12]:

$$\begin{aligned}\mu_{nf}&=\frac{\mu_f}{(1-\varphi)^{2.5}},\\ \nu_{nf}&=\frac{\mu_{nf}}{\rho_{nf}},\\ \rho_{nf}&=(1-\varphi)\rho_f+\varphi\rho_s+\varphi\rho_s,\\ (\rho\beta)_{nf}&=(1-\phi_{nf})(\rho\beta)_f+\varphi(\rho\beta)_s,\\ (\rho C_p)_{nf}&=(1-\varphi)(\rho C_p)_f+\varphi(\rho C_p)_s,\\ \kappa_{nf}&=\frac{(\kappa_s+2\kappa_f)-2\varphi(\kappa_f-\kappa_s)}{(\kappa_s+2\kappa_f)+2\varphi(\kappa_f-\kappa_s)}.\end{aligned} \tag{7}$$

Here the following notation applies: *φ-nanoparticle volume fraction; μ_{nf} -nanofluid dynamic viscosity; μ_f -base fluid dynamic viscosity; β_{nf} -nanofluid thermal expansion coefficient; β_f - base fluid thermal expansion coefficient; βs-nanoparticle thermal expansion coefficient; ρ_f - base fluid density; ρ_s-nanoparticle (copper) density; ρ_{nf} -nanofluid density; ν_{nf} -nanofluid kinematic viscosity; ν_f -base fluid kinematic viscosity; κ_{nf} -nanofluid thermal conductivity.* The equations (1-4) are highly coupled, non-linear partial differential equations. The equation (4)

is of order *n*. To solve these equations efficiently and easily, we convert them into ordinary differential equations, using suitable similarity transformation.

$$\eta = (\frac{\Omega sin\alpha}{\nu})^{1/2} z, r = xsin\alpha, u = x\Omega sin\alpha f', v = x\Omega sin\alpha g, w = (\nu\Omega sin\alpha)^{1/2} f,$$
$$\theta = \frac{T-T_\infty}{T_w-T\infty}, \phi = \frac{C-C_\infty}{C_w-C_\infty}, T_w - T_\infty = \frac{(T_L-T_\infty)x}{L}, C_w - C_\infty = \frac{(C_L-C_\infty)x}{L}. \quad (8)$$

Similarity transformations (8) are used to simplify the equations (1-5), thus facilitating the solution. Buckingham's π theorem is applied to deduce similarity transformations (8). Using (7) and (8), equations (1-5) become:

$$f''' = \frac{1}{a_1}[2f'^2 + ff'' + \frac{a_1 f'}{K} + \frac{Mf'}{a_2} - \frac{a_3}{a_2} Ri(\theta + N\phi)], \quad (9)$$

$$g'' = \frac{1}{a_1}[2f'g + fg' + \frac{a_1 g}{K} + \frac{Mg}{a_2}], \quad (10)$$

$$\theta'' = \frac{a_5 Pr}{(a_5 PrDuSr - a_4)}[Duf'Sc\phi + Du\gamma\phi^n + fScDu\phi' - f'\theta - f\theta'], \quad (11)$$

$$\phi'' = \frac{1}{(a_5 PrDuSr - a_4)}[a_5 Prf'Sr\theta - a_4 f'Sc\phi + a_5 Prf'Sr\theta' - a_4\gamma\phi^n - a_4 fSc\phi']. \quad (12)$$

The transformed boundary conditions:

$$f = 0, g = 1, f' = 0, \theta = 1, \phi = 1 \quad \text{at} \quad \eta = 0,$$
$$f' \to 0, g \to 0, \theta \to 0, \phi \to 0 \quad \text{as} \quad \eta \to \infty. \quad (13)$$

Here primes denote derivatives with respect to the normalized coordinate, *η*; Here:

$$M = \frac{\sigma_{nf} B_o^2}{\rho_f \Omega sin\alpha}, K = \frac{\nu_f}{K^* \Omega sin\alpha}, Pr = \frac{(\mu C_p)_f}{\kappa_f}, \gamma = \frac{k_r}{\Omega sin\alpha}(C - C_\infty)^{n-1}, Sc = \frac{\nu}{D_m},$$
$$N = \frac{T_w - T_\infty}{C_w - C_\infty}, Gr_L = \frac{g\beta_f cos\alpha (T_w - T_\infty) L^3}{\nu^2}, Re_L = \frac{\Omega L^2 sin\alpha}{\nu_f}, Du = \frac{D_m K_t}{C_s C_p \nu} \frac{C_w - C_\infty}{T_w - T_\infty},$$
$$Ri = \frac{Gr_L}{(Re_L)^2}, Sr = \frac{D_m K_t}{T_m} \frac{T_w - T\infty}{C_w - C_\infty}, a_1 = \frac{1}{(1-\varphi)^{2.5}} \frac{1}{(1-\varphi) + \varphi(\frac{\rho_s}{\rho_f})}, a_2 = (1-\varphi) + \varphi(\frac{\rho_s}{\rho_f}),$$
$$a_3 = (1-\varphi) + \varphi(\frac{(\rho\beta)_s}{(\rho\beta)_f}), a_4 = \frac{(\kappa_s + \kappa_f) - 2\varphi(\kappa_f - \kappa_s)}{(\kappa_s + \kappa_f) + 2\varphi(\kappa_f + \kappa_s)} \cdot \frac{1}{\kappa_f}, a_5 = ((1-\varphi)(\rho C_p)_f + \varphi(\rho C_p)_s). \quad (14)$$

Where *K-inverse permeability parameter; Gr_L- thermal Grashof number; Re_L-rotational Reynolds number; Ri - Richardson number; Du-Dufour number; Sr-Soret number; T_w-cone wall temperature; T_∞-free stream temperature; L-cone slant height; C_w-concentration at wall (cone surface); N is buoyancy ratio parameter, M-dimensionless magnetic field parameter; C_w-cone surface (wall) concentration; γ-dimensionless chemical reaction parameter; Pr-*

Prandtl number; Sc-Schmidt number; a_1,a_2,a_3,a_4 and a_5 are coefficients based on the Tiwari-Das volume fraction relations. Local skin friction coefficient in the *tangential* direction is:

$$Cf_x = \frac{\mu_{nf}\left(\frac{\partial u}{\partial z}\right)_{z=0}}{\rho_f {v_0}^2} \Rightarrow Cf_x(1-\varphi)^{2.5} = f''(0). \tag{15}$$

Local skin friction coefficient in *circumferential (azimuthal)* direction is:

$$Cf_y = \frac{\mu_{nf}\left(\frac{\partial v}{\partial z}\right)_{z=0}}{\rho_f {v_0}^2} \Rightarrow Cf_y(1-\varphi)^{2.5} = g'(0). \tag{16}$$

Local Nusselt number (heat transfer rate at the cone surface) is:

$$Nu_x = \frac{-x\kappa_{nf}\left(\frac{\partial T}{\partial z}\right)_{z=0}}{K_f(T_w - T_\infty)} \Rightarrow \frac{Nu_x}{Re_x}\frac{\kappa_f}{\kappa_{nf}} = -\theta'(0). \tag{17}$$

Local Sherwood number (mass transfer rate at the cone surface) is:

$$Sh_x = \frac{-xD_m\left(\frac{\partial C}{\partial z}\right)_{z=0}}{D_m(C_w - C_\infty)} \Rightarrow \frac{Sh_x}{Re_x} = -\phi'(0). \tag{18}$$

Thermodynamical properties of Cu and H_2O are displayed in **Table-1** and extracted from [43].

Table 1: Thermophysical properties of water and copper nanoparticles

Thermodynamical properties	Water	Copper
$C_p(J/(kgK))$	4179	385
$\rho(kg/m^3)$	997.1	8933
$\kappa(W/mK)$	0.613	400
$\beta * 10^{-5}(K^{-1})$	21	1.67

3 METHOD OF SOLUTION AND VALIDATION

The dimensionless boundary value problem defined by Eqns. (9-12) along with boundary conditions (13) is non-linear, coupled and features multi-degree and n^{th} order terms. Analytical solutions are intractable. A computational approach is therefore adopted to provide efficient solutions quickly. The numerical approach uses MATLAB bvp4c package to calculate the solution. This solver implements the exceptionally stable and highly convergent Runge-Kutta

method with shooting technique. An overview of the procedure is given in **Fig. 2**. Further details are provided in [44-46] including convergence criteria, stepping distances etc.

Consider: *f = f(1); f ' = f(2); f '' = f(3); g = f(4); g ' = f(5); θ = f(6); θ ' = f(7); ϕ = f(8); ϕ ' = f(9);*

We use these functions to compute the solutions to the differential equations using bvp4c in relevance to the boundary conditions. The non-linear differential equations (9-12) are cast as 1st order equations:

$$f' = f(2) \tag{19}$$

$$f'' = f(3) \tag{20}$$

$$f''' = \frac{1}{(a_1)}[\frac{a_1 f(2)}{K} - (f(1))^2 + f(1)f(3) + \frac{Mf(2)}{a_2} + 2\frac{a_3}{a_2}Ri(f(6) + Nf(8))] \tag{21}$$

$$g' = f(5) \tag{22}$$

$$g'' = \frac{1}{(a_1)}[\frac{a_1 f(4)}{K} - f(2)f(4) + f(1)f(5) + \frac{Mf(4)}{a_2}] \tag{23}$$

$$\theta' = f(7) \tag{24}$$

$$\theta'' = \frac{a_5 Pr}{(a_5 PrDuSr - a_4)}[\gamma Du(f(8)^n) + DuScf(1)f(9) + DuScf(2)f(8) - f(2)f(6) - f(1)f(7)] \tag{25}$$

$$\phi' = f(9) \tag{26}$$

$$\phi'' = \frac{1}{(a_5 PrDuSr - a_4)}[a_5 PrSrf(1)f(7) - a_4\gamma(f(8)^n) + a_5 PrSrf(2)f(6) - a_4 Scf(2)f(8) - a_4 Scf(1)f(9)]. \tag{27}$$

The shooting technique effectively converts the *boundary* value problem into an equivalent *initial* value problem. So, we redefine the boundary conditions as follows:

$$\begin{aligned} f(1) = 0, f(2) = 0, f(4) = 1, f(6) = 1, f(8) = 1 \quad at \quad \eta = 0 \\ f(2) = 0, f(4) = 0, f(6) = 0, f(8) = 0 \quad at \quad \eta \to \infty. \end{aligned} \tag{28}$$

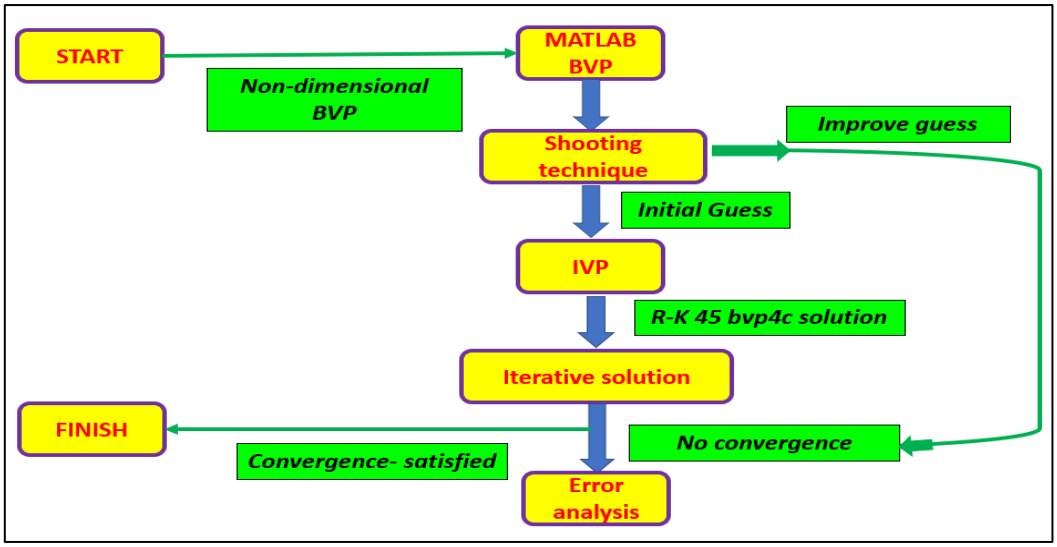

Fig 2: MATLAB bvp4c numerical methodology

The MATLAB bvp4c solver divides the given boundary into mesh points and estimates the solution at the divided mesh intervals. To confirm the accuracy of the solutions, benchmarking with the earlier results of Verma *et. al* [42] is performed. Table 2 provides the comparison of our results with Verma *et. al* [42] for the special case wherein $Ri = 0$; $N = 0$ *(buoyancy effects negated);* $K = 0$ *(infinite permeability i. e. vanishing solid matrix fibres);* $Pr = 0.72$ *(air);* $Du = 0$; $Sc = 0$; $\gamma = 0$; $Sr = 0$; $\phi_0 = 0$ (mass transfer, Soret/Dufour and nanoparticle effects negated). Our results are in good agreement with the existing literature justifying confidence in the MATLAB bvp4c code implemented.

Table 2 Comparison of present results with Verma *et. al* [42] with $Ri = 0$; $N = 0$; $K = 0$; $Pr = 0.72$; $Du = 0$; $Sc = 0$; $\gamma = 0$; $Sr = 0$; $\phi_0 = 0$.

M	Verma et. al [42] $-g'(0)$	Present results $-g'(0)$
0.5	0.8488	0.8475
1.0	1.0691	1.0690
2.0	1.4421	1.4374
3.0	1.7477	1.7416
4.0	2.0103	2.004

4 RESULTS AND DISCUSSION

We have obtained extensive numerical solutions for the boundary value problem. Copper (Cu) nanoparticles are suspended in H_2O with 0.15 (15%) prescribed as the copper metallic nanoparticle volume fraction to maximize thermal conductivity enhancement in the coating.

The impacts of *M, K, Ri, Du, Sr, Sc, γ, n* on all key boundary layer characteristics i.e. f, *g, f' , f''(0), g' (0), −θ ' (0), ϕ' (0)* are presented in **Figures 3-26**. Furthermore skin friction coefficients i.e. *f ''(0), g ' (0)*, Nusselt number function, *−θ ' (0)* and Sherwood number function, *−ϕ ' (0)* with variation in selected parameters i.e. *γ, Du, So and n* are documented in **Tables 3-5** respectively. In the computations, the default parameter values are: *Ri = 1 (equivalence of thermal Grashof and rotational Reynolds number); N = 1; M = 2; P r = 6.785; Du = 5; Sc = 0.6; n = 1; Sr = 5; γ = 1; K = 1*. These are representative of actual magnetic nanomaterial spin coating processes [10, 31, 33]. Slow rotation of the cone is considered since this achieves improved deposition and consistency of coatings [27] and avoids boundary layer separation. A major focus of the simulations is to determine the influence of n^{th} order chemical reaction impacts on transport characteristics and the collective influence of other thermal, magnetic and solutal parameters.

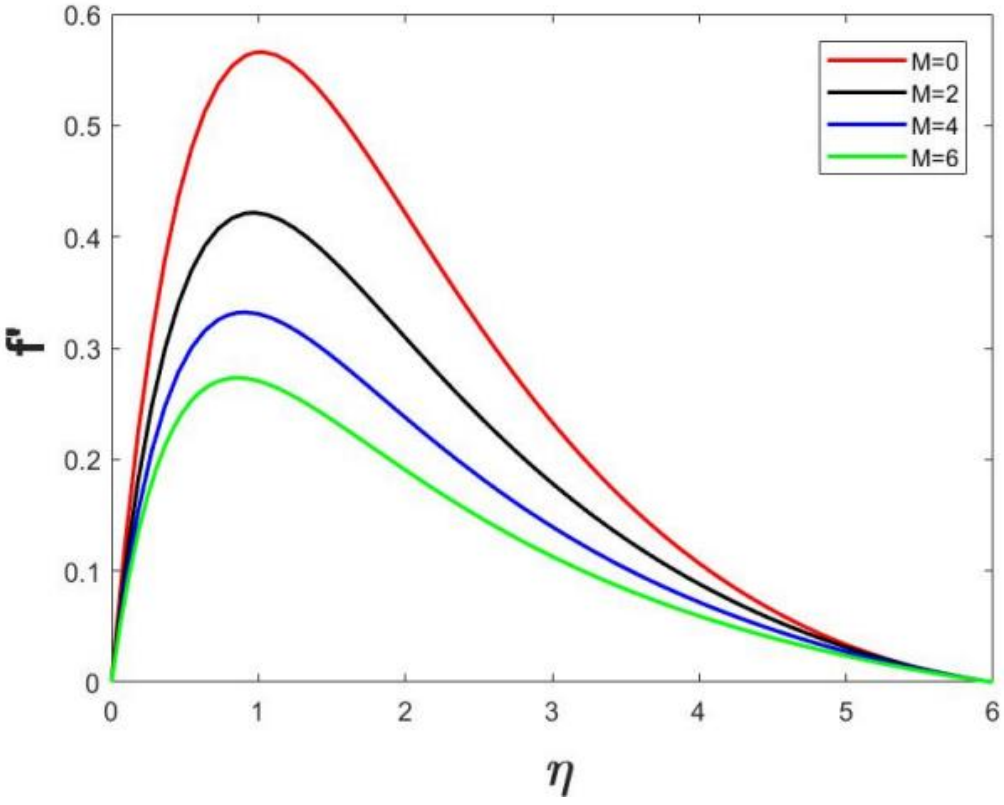

Fig. 3 Tangential velocity variation with magnetic body force parameter, *M*

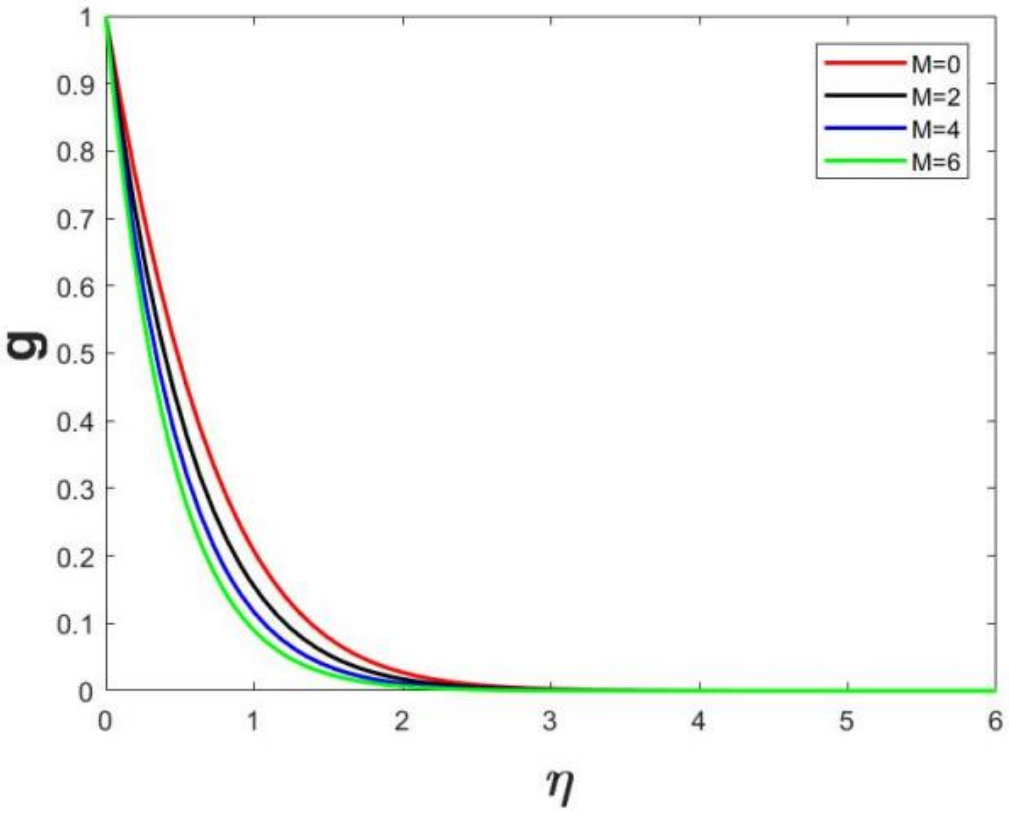

Fig. 4: Circumferential (azimuthal) velocity variation with magnetic body force parameter, *M*

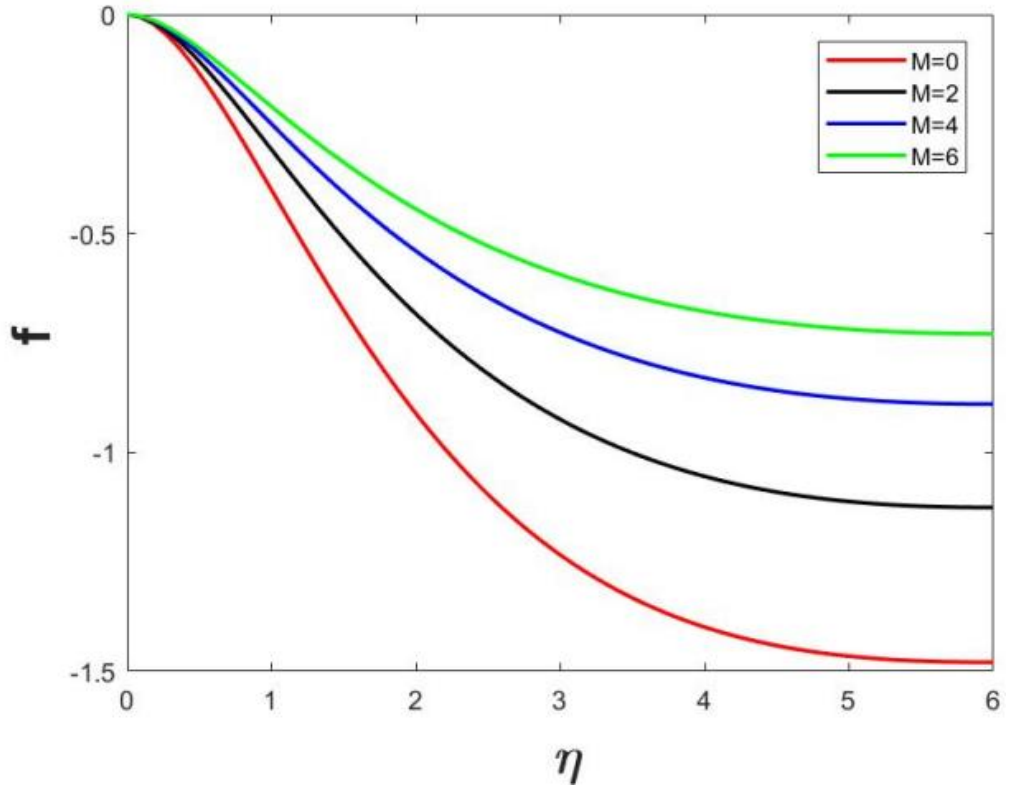

Fig. 5 Normal velocity variation with magnetic body force parameter, *M*

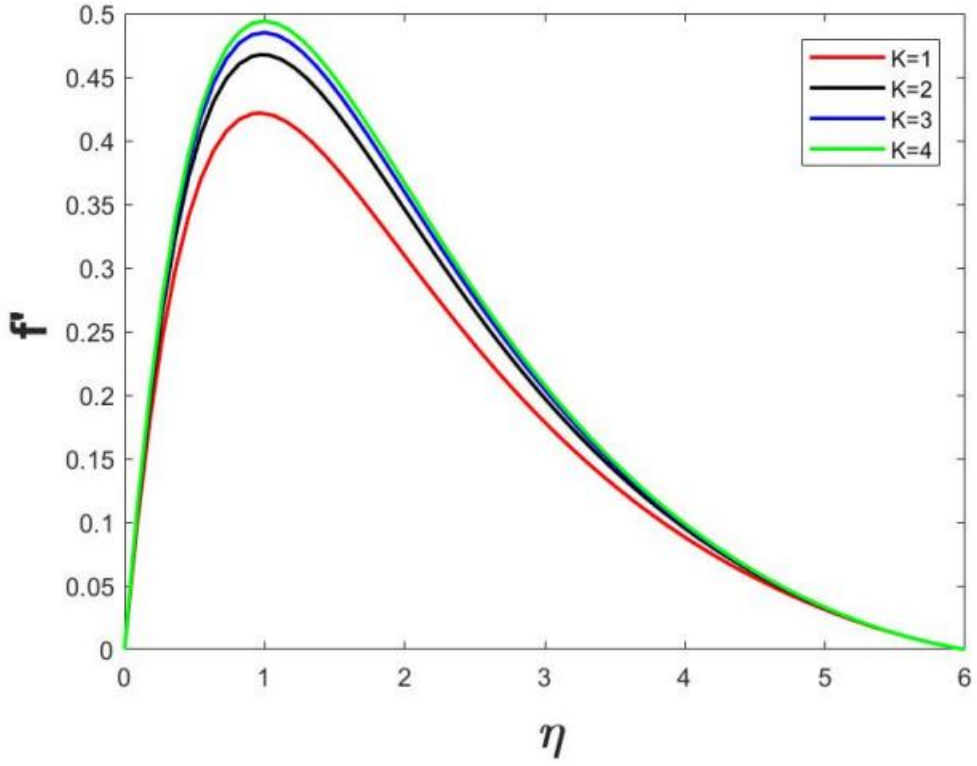

Fig. 6 Tangential velocity variation with permeability parameter, *K*

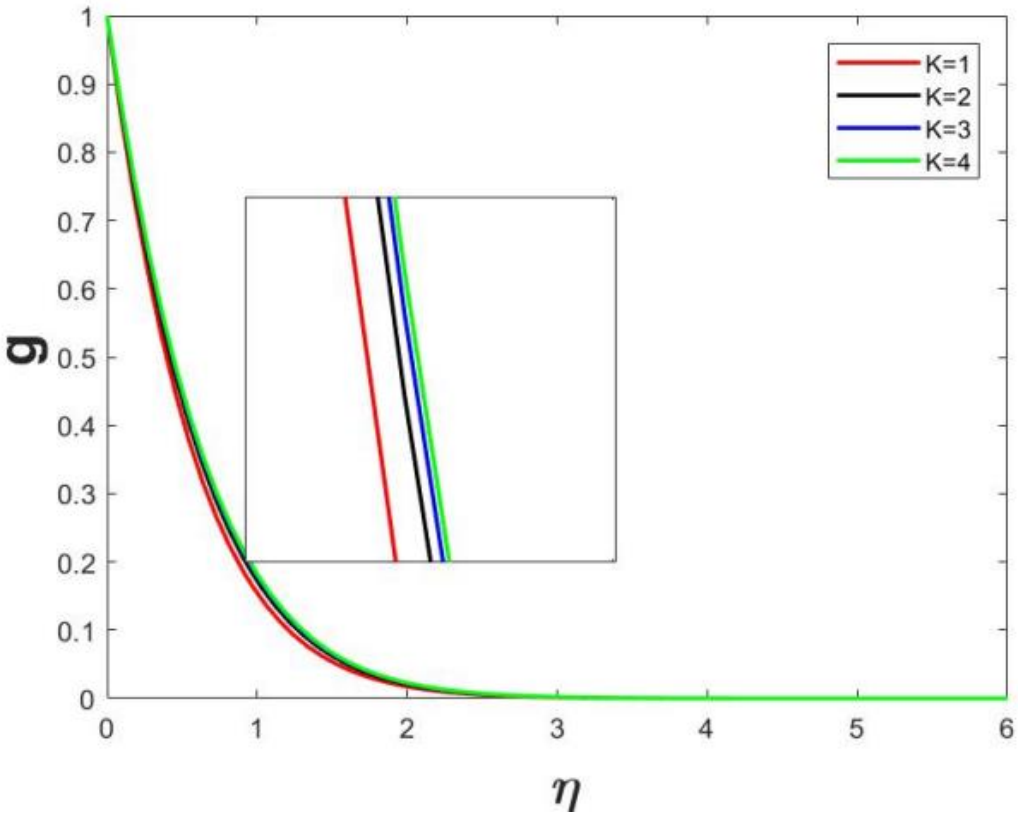

Fig. 7 Circumferential velocity variation with permeability parameter, *K*

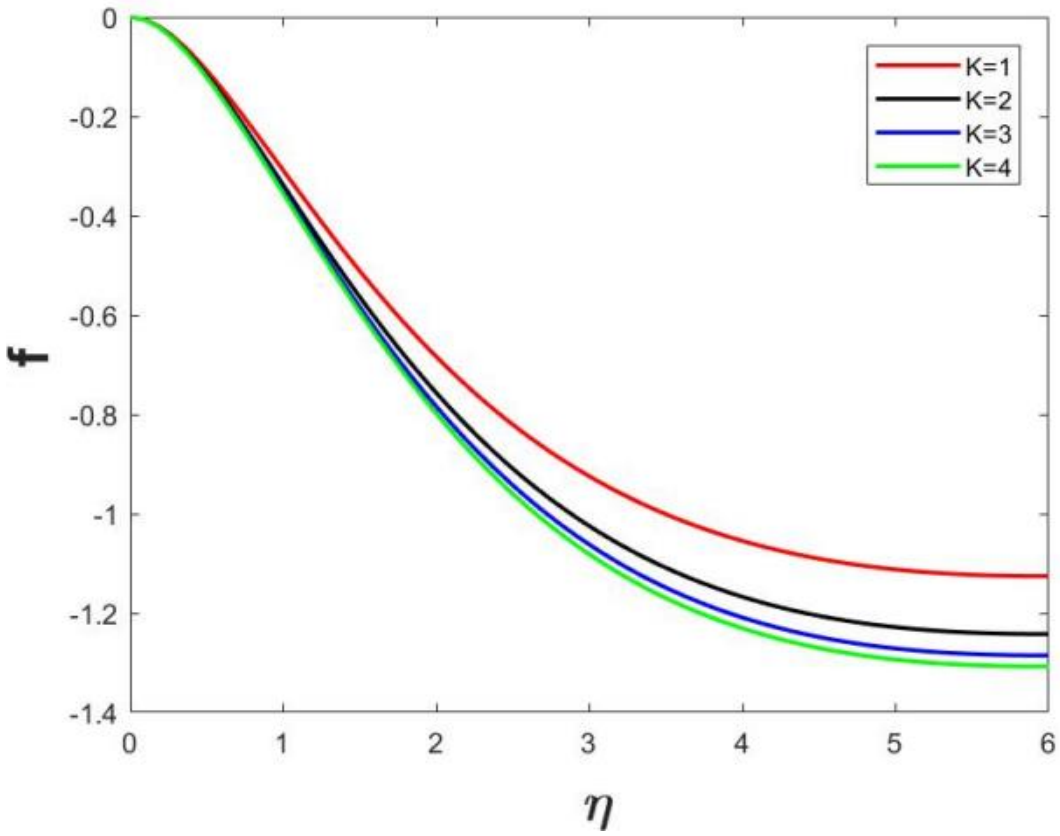

Fig. 8 Normal velocity variation with permeability parameter, *K*

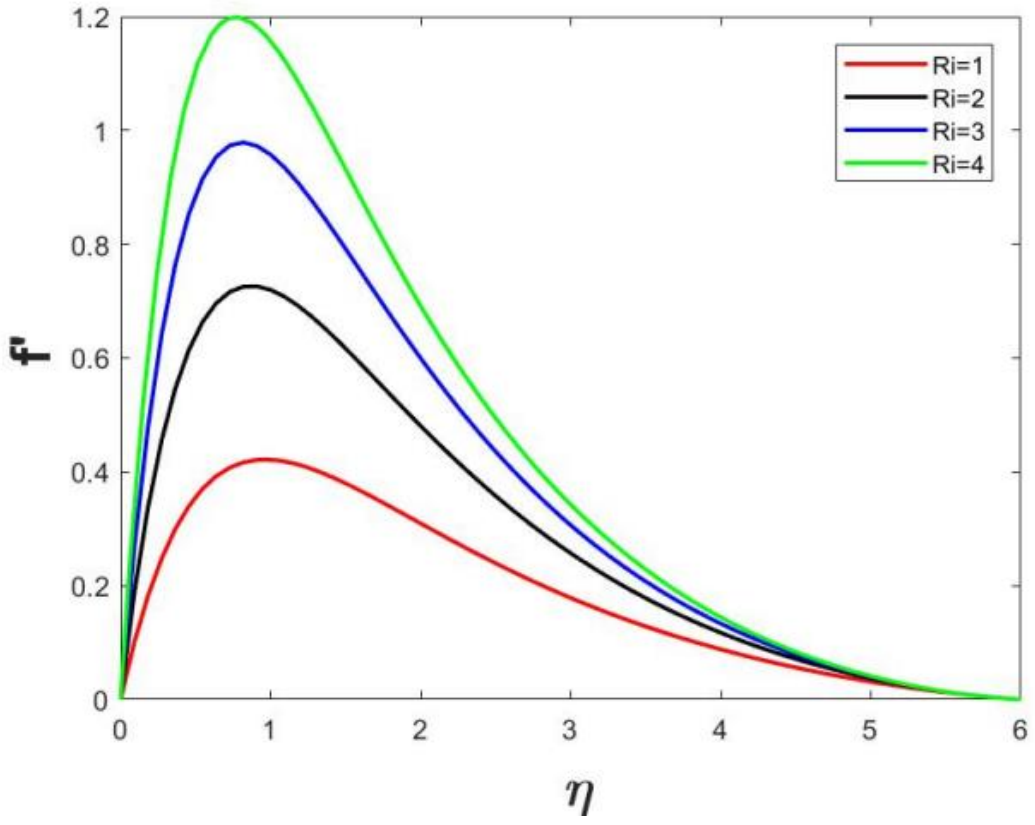

Fig. 9 Tangential velocity variation with Richardson number, *Ri*

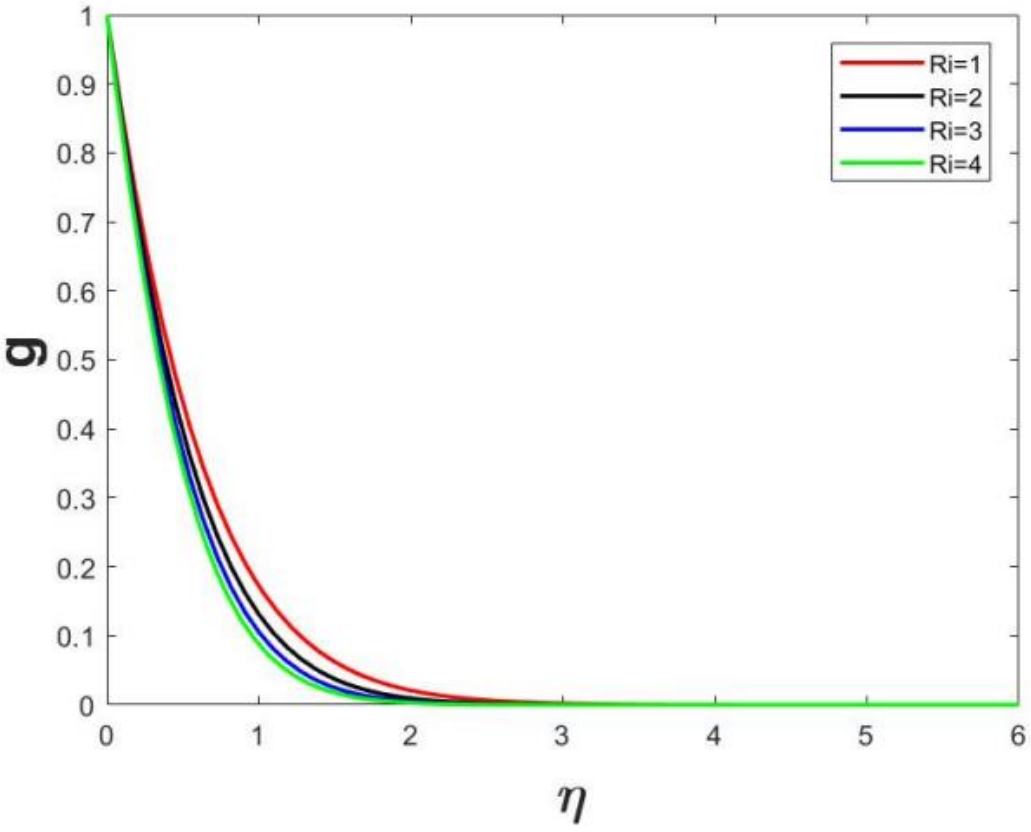

Fig. 10 Circumferential velocity variation with Richardson number, *Ri*

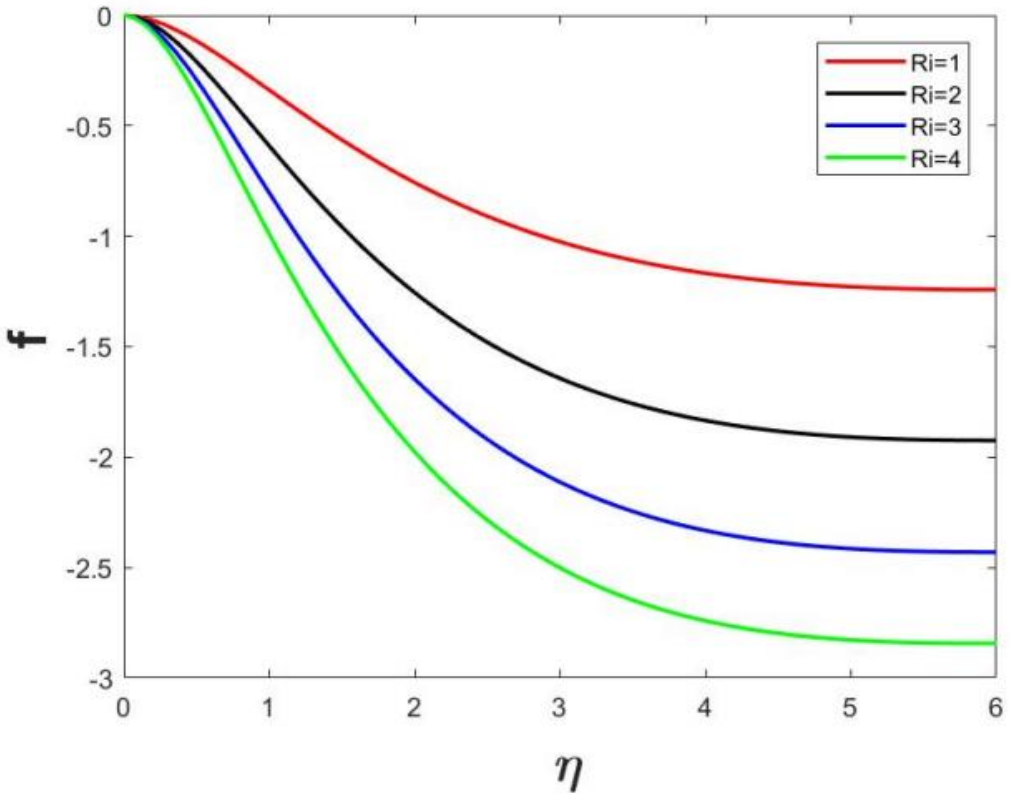

Fig. 11 Normal velocity variation with Richardson number, *Ri*

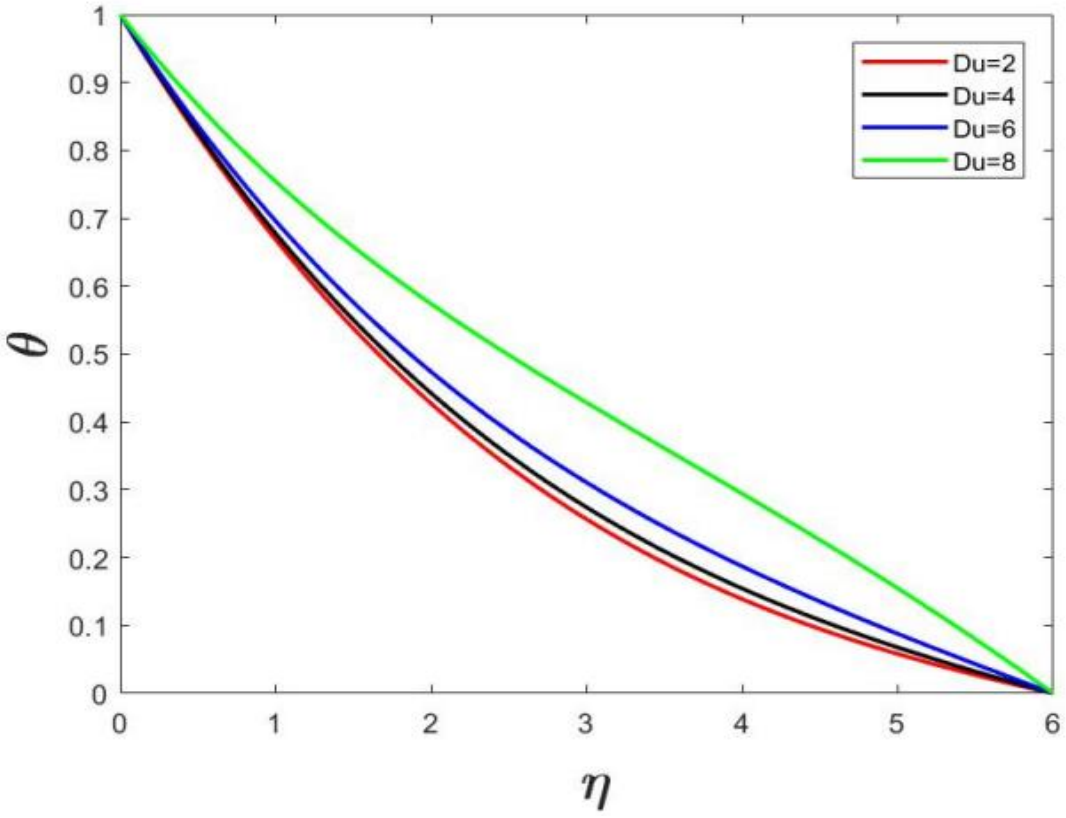

Fig. 12 Temperature variation with Dufour number, *Du*

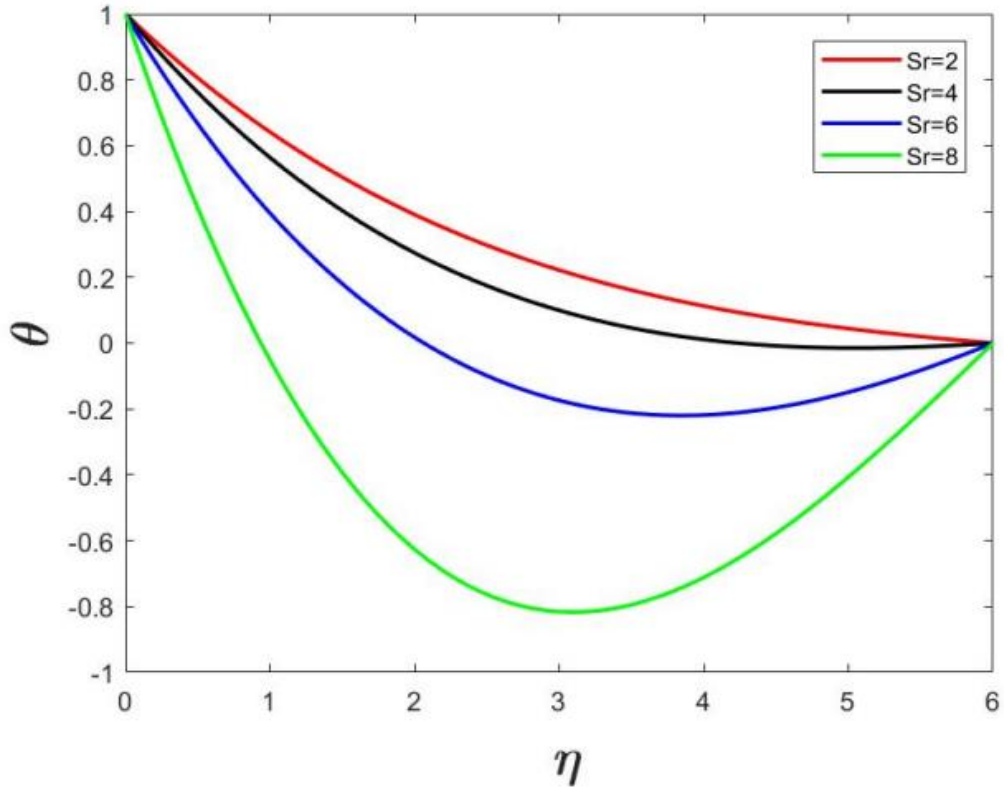

Fig. 13 Temperature variation with Soret number, *Sr*

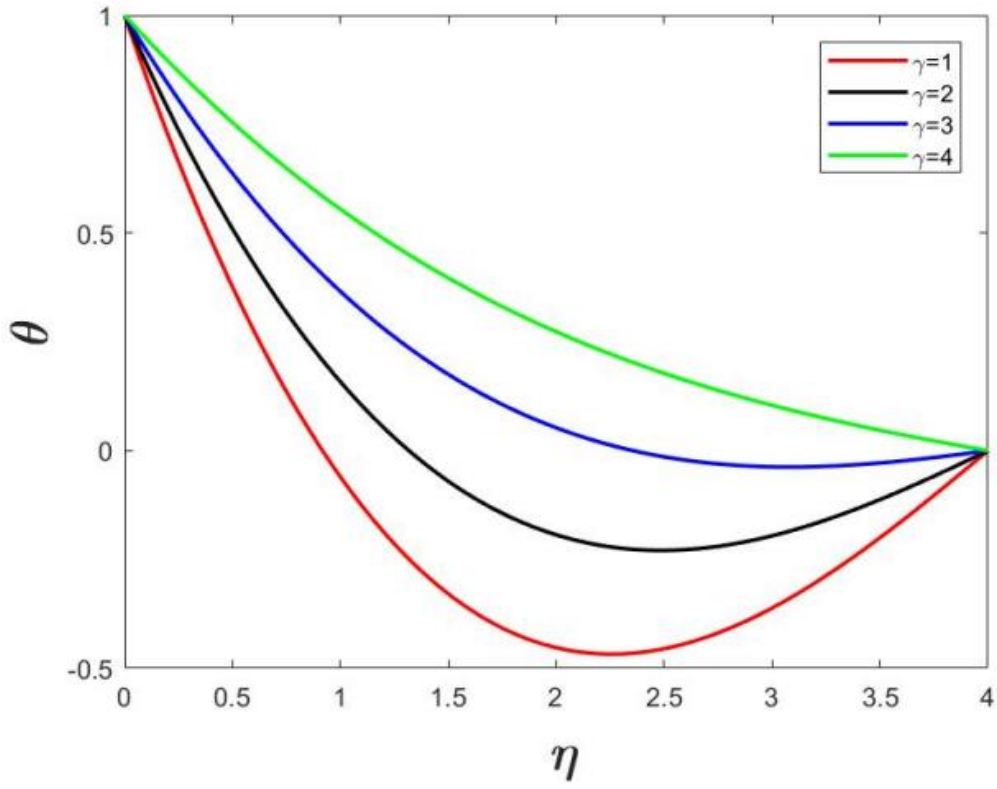

Fig. 14 Temperature variation with chemical reaction parameter, γ

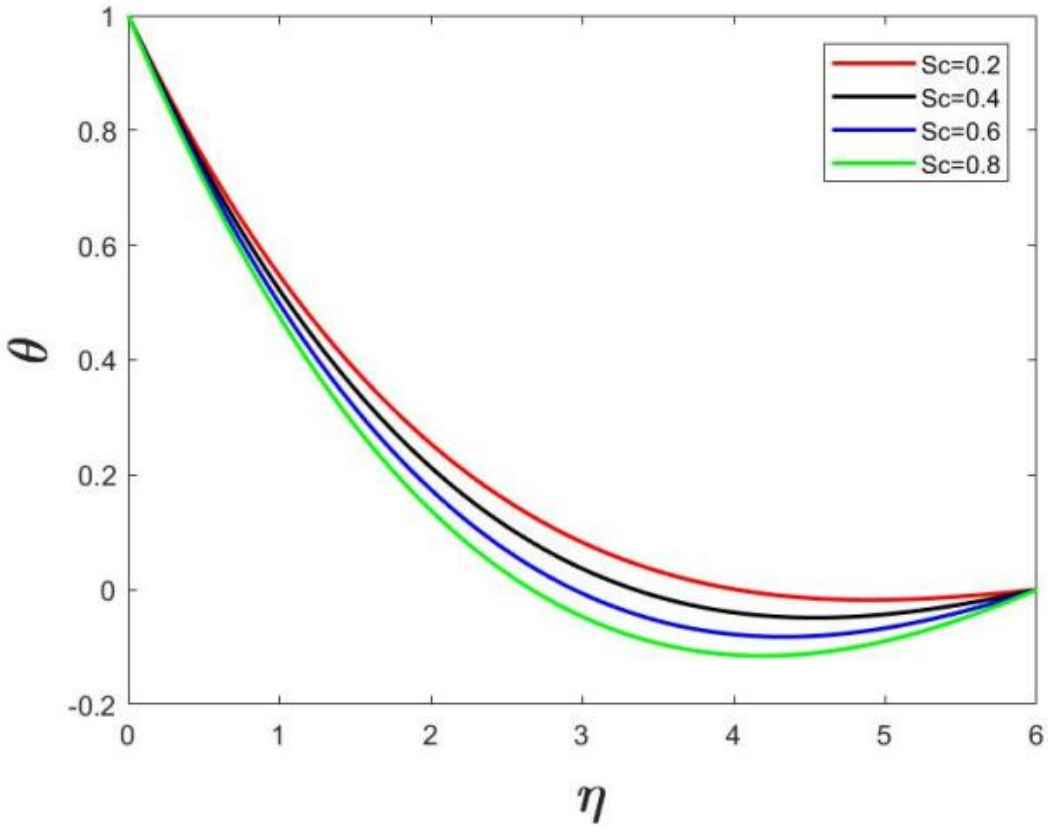

Fig. 15 Temperature variation with Schmidt number, *Sc*

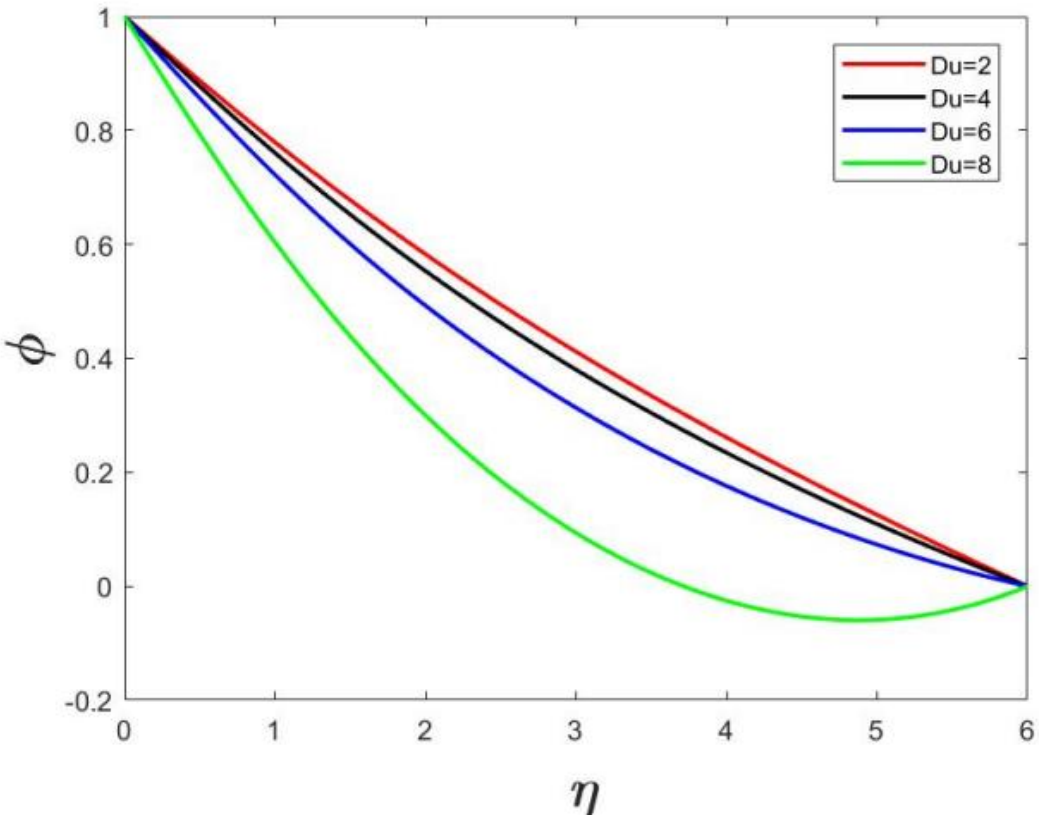

Fig. 16 Concentration variation with Dufour number, *Du*

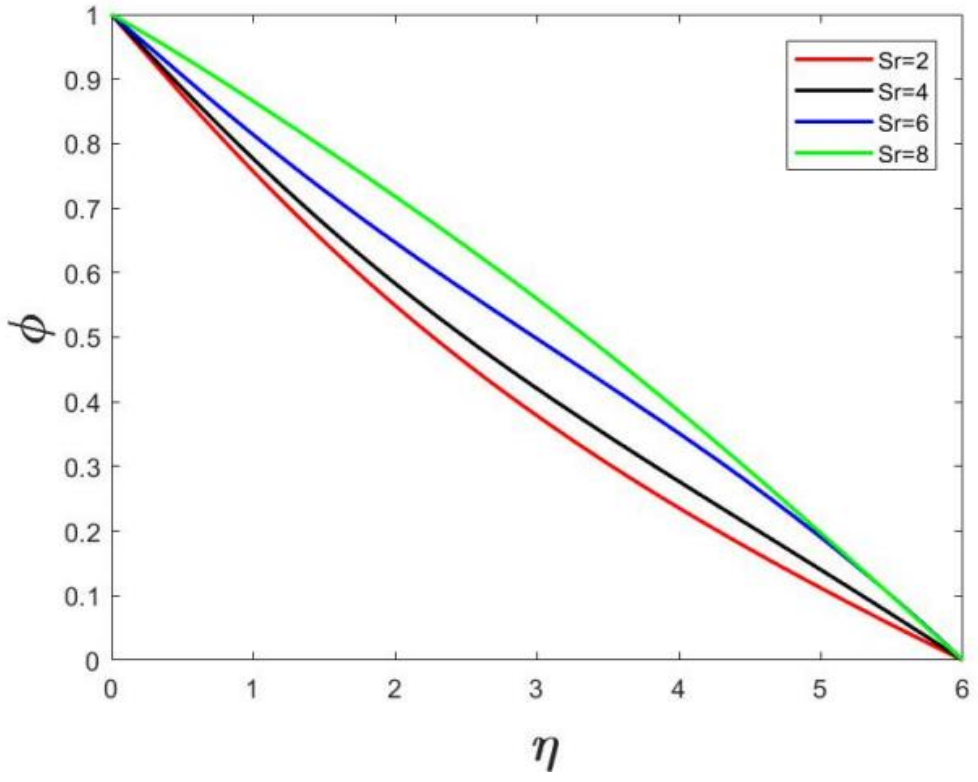

Fig. 17 Concentration variation with Soret number, *Sr*

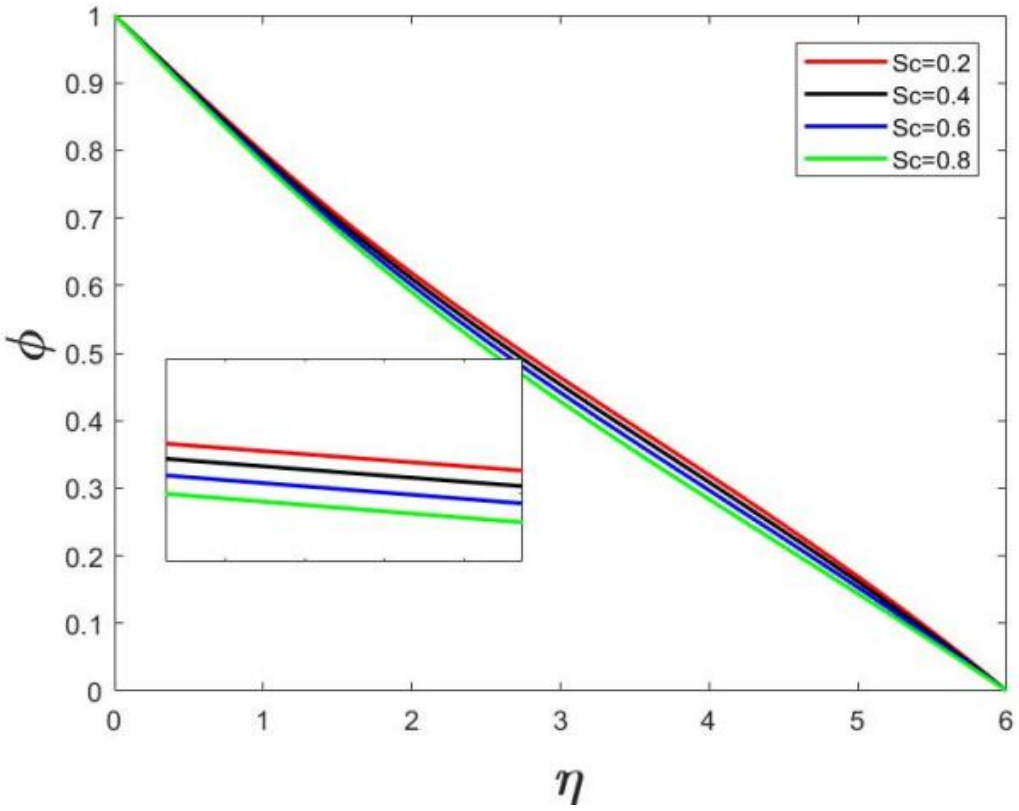

Fig. 18 Concentration variation with Schmidt number, *Sc*

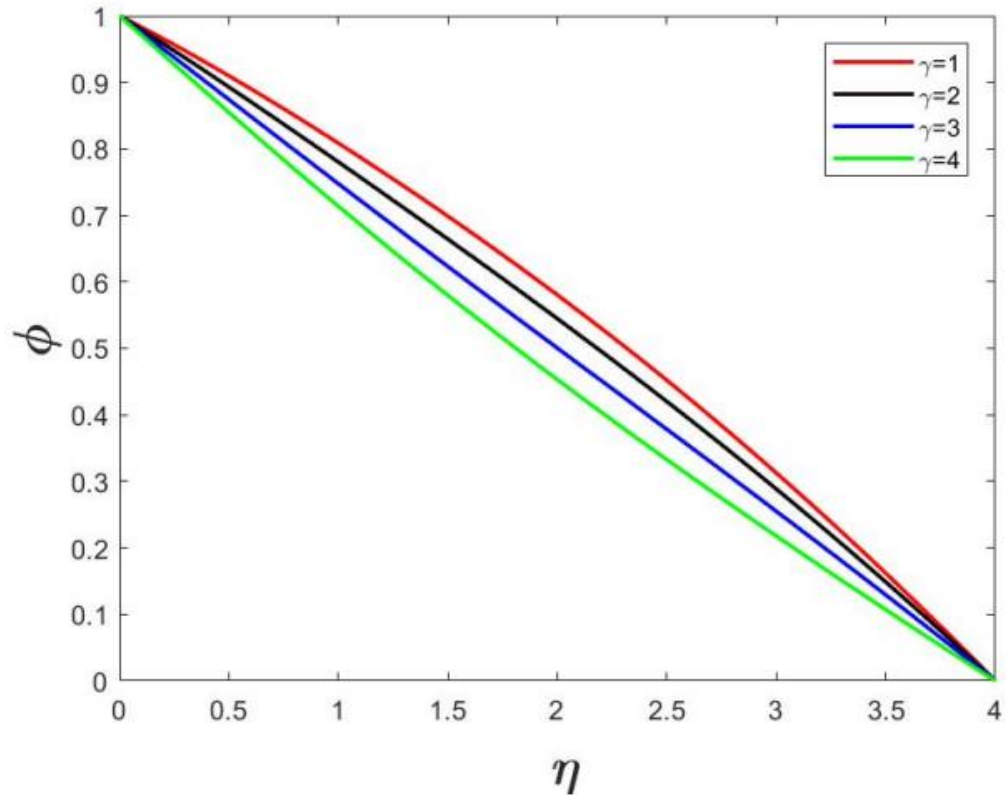

Fig. 19 Concentration variation with chemical reaction parameter, γ

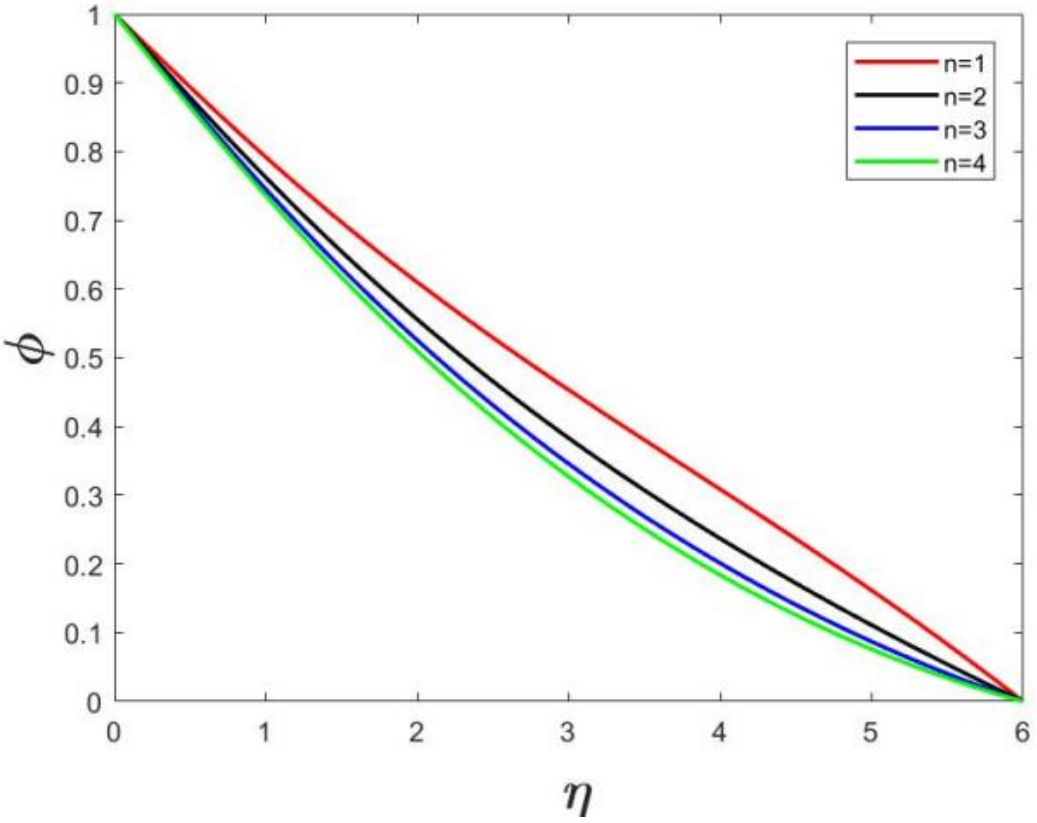

Fig. 20 Concentration variation with order of chemical reaction, *n*

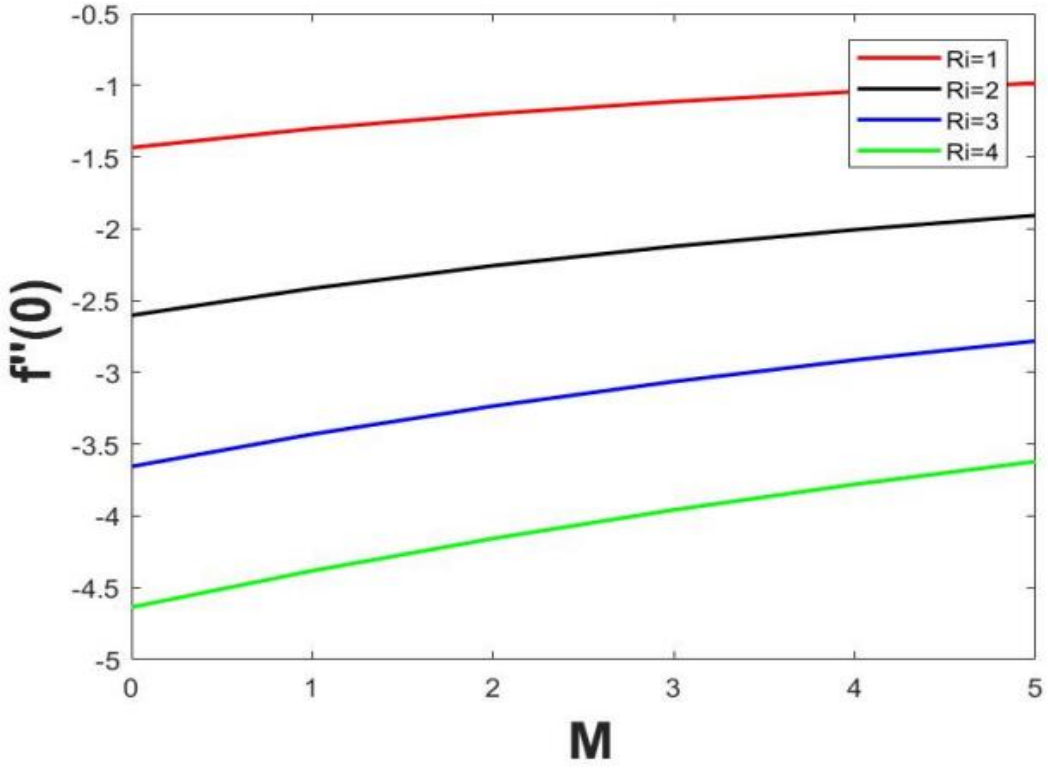

Fig. 21 Tangential skin friction coefficient variation with Richardson number *Ri* and magnetic parameter, *M*

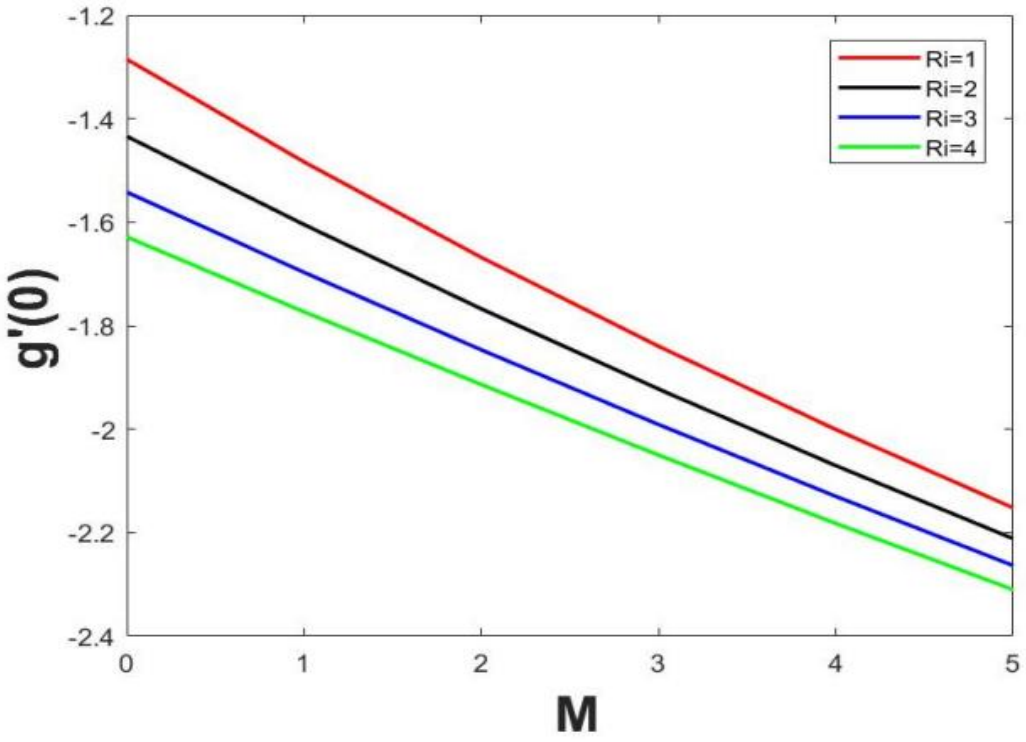

Fig. 22 Circumferential skin friction coefficient variation with Richardson number *Ri* and magnetic parameter, *M*

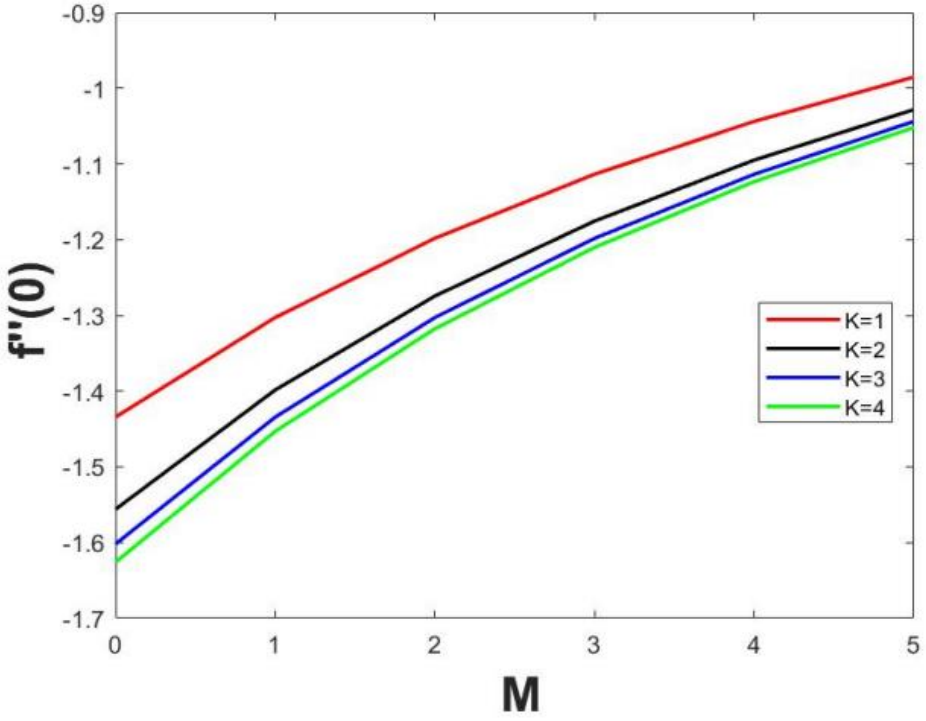

Fig. 23 Tangential skin friction coefficient variation with permeability parameter *K* and magnetic parameter, *M*

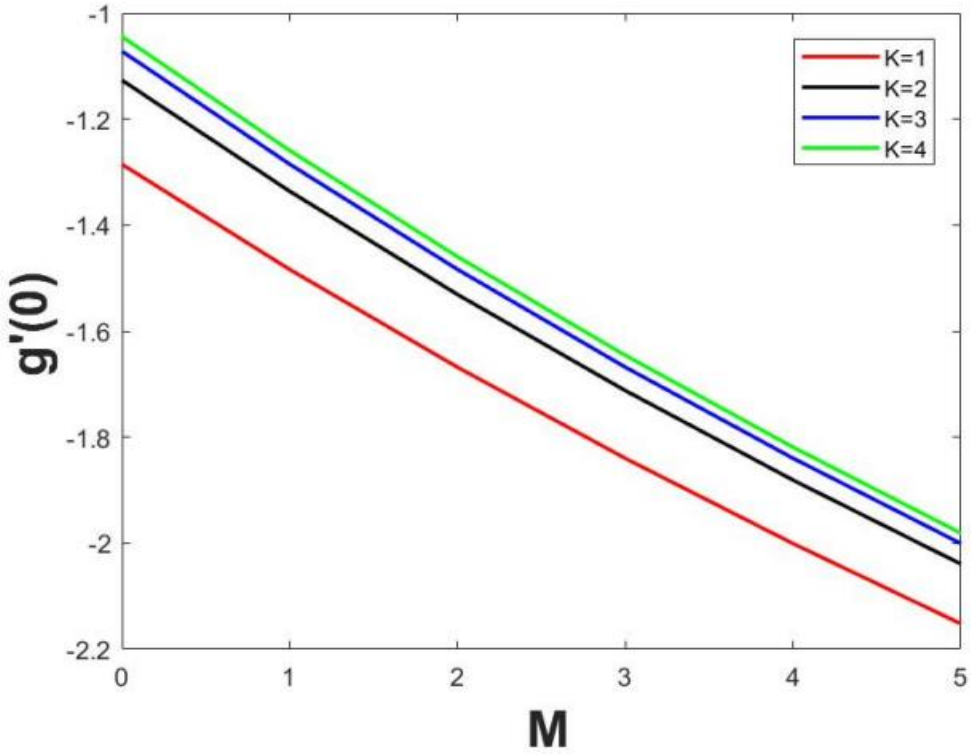

Fig. 24 Circumferential skin friction coefficient variation with permeability parameter *K* and magnetic parameter, *M*

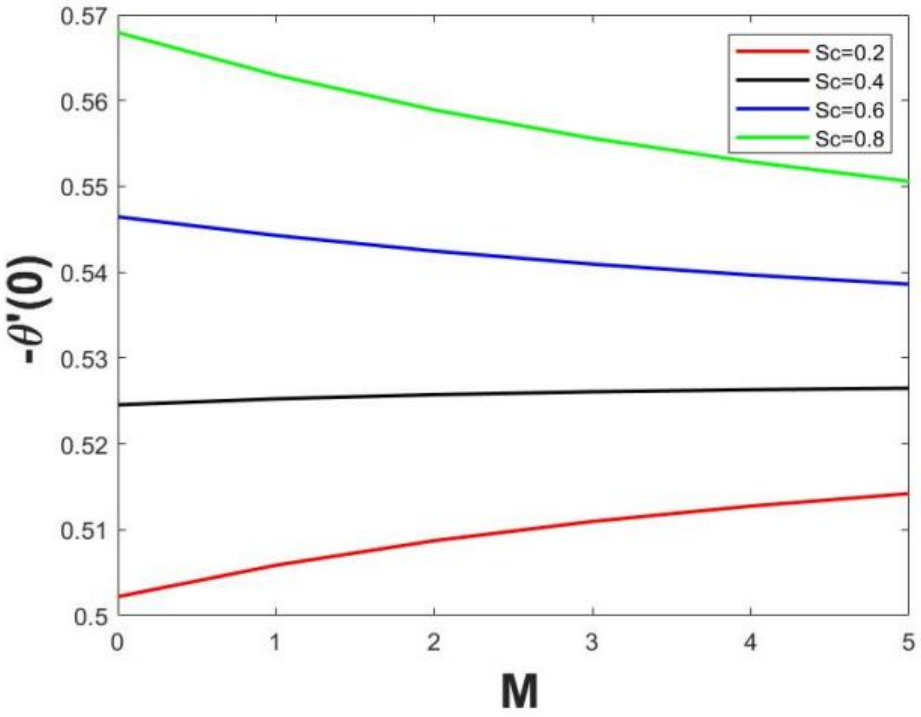

Fig. 25 Nusselt number variation for with Schmidt number *Sc* and magnetic parameter, *M*

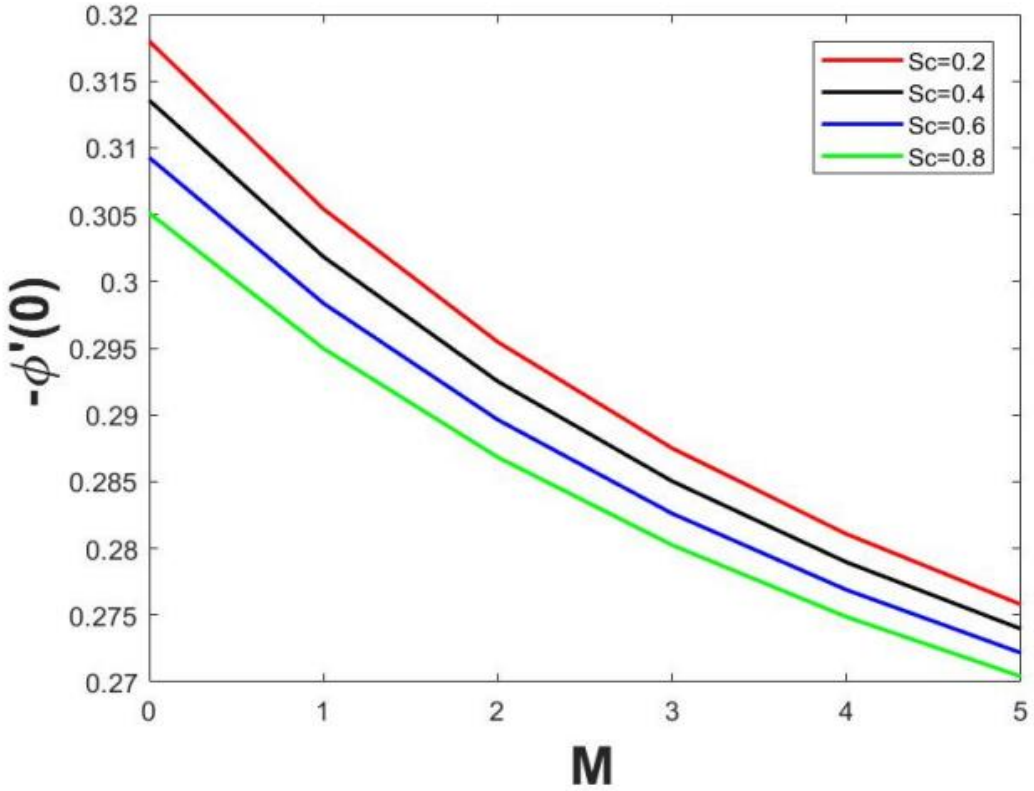

Fig. 26 Sherwood number variation with Schmidt number *Sc* and magnetic parameter, *M*

Table 3 Variation in $f''(0)$, $g'(0)$, $-\theta'(0)$, $-\phi'(0)$ for $\gamma = 1, 2, 3, 4$ and $n = 1, 2, 3, 4$.

γ	n	$f''(0)$	$g'(0)$	$-\theta'(0)$	$-\phi'(0)$
	1	-1.100644	-1.653539	0.204664	0.858041
1	2	-1.144195	-1.660511	0.214461	0.925650
	3	-1.165975	-1.663885	0.219855	1.030279
	4	-1.178597	-1.665777	0.223325	1.219337
	1	-1.049879	-1.646402	0.181648	1.117134
2	2	-1.107235	-1.655377	0.196327	1.224231
	3	-1.138304	-1.660144	0.204697	1.386979
	4	-1.156969	-1.662924	0.210186	1.671848
	1	-1.017763	-1.642113	0.163546	1.329533
3	2	-1.082087	-1.651971	0.181822	1.466534
	3	-1.118769	-1.657548	0.192409	1.672769
	4	-1.141334	-1.660891	0.199423	2.028735
	1	-0.994580	-1.639145	0.148149	1.513741
4	2	-1.063074	-1.649449	0.169399	1.675560
	3	-1.103640	-1.655567	0.181816	1.917809
	4	-1.129041	-1.659310	0.190094	2.332761

Table 4 Variation in $f''(0)$, $g'(0)$, $-\theta'(0)$, $-\phi'(0)$ for $Du = 1, 2, 3, 4$ and $n = 1, 2, 3, 4$.

Du	n	$f''(0)$	$g'(0)$	$-\theta'(0)$	$-\phi'(0)$
	1	-1.112577	-1.655212	0.245093	0.769301
1	2	-1.154676	-1.662032	0.247048	0.828430
	3	-1.175703	-1.665329	0.248099	0.919930
	4	-1.187970	-1.667195	0.248763	1.085747
	1	-1.109907	-1.654834	0.236081	0.788610
2	2	-1.152349	-1.661693	0.239807	0.849601
	3	-1.173554	-1.665009	0.241837	0.943986
	4	-1.185907	-1.666883	0.243134	1.114916
	1	-1.107045	-1.654432	0.226404	0.809648
3	2	-1.149843	-1.661329	0.232017	0.872657
	3	-1.171233	-1.664664	0.235091	0.970166
	4	-1.183674	-1.666545	0.237062	1.146628
	1	-1.103968	-1.654001	0.215969	0.832683
4	2	-1.147134	-1.660936	0.223600	0.897888
	3	-1.168716	-1.664291	0.227791	0.998796
	4	-1.181246	-1.666177	0.230485	1.181274

Table 5 Variation in $f''(0)$, $g'(0)$, $-\theta'(0)$, $-\phi'(0)$ for $Sr = 1, 2, 3, 4$ and $n = 1, 2, 3, 4$.

Sr	n	$f''(0)$	$g'(0)$	$-\theta'(0)$	$-\phi'(0)$
1	1	-1.117939	-1.656057	0.211150	0.778236
	2	-1.157632	-1.662462	0.219702	0.836797
	3	-1.177406	-1.665550	0.224390	0.927548
	4	-1.188903	-1.667292	0.227401	1.092172
2	1	-1.114046	-1.655486	0.209738	0.795543
	2	-1.154623	-1.662022	0.218563	0.856081
	3	-1.174856	-1.665177	0.223405	0.949866
	4	-1.186612	-1.666954	0.226517	1.119837
3	1	-1.109889	-1.654879	0.208200	0.814439
	2	-1.151399	-1.661553	0.217321	0.877125
	3	-1.172117	-1.664777	0.222331	0.974205
	4	-1.184146	-1.666591	0.225552	1.149980
4	1	-1.105434	-1.654231	0.206516	0.835170
	2	-1.147934	-1.661051	0.215960	0.900202
	3	-1.169167	-1.664348	0.221153	1.000880
	4	-1.181483	-1.666200	0.224493	1.182988

Figure 3-5 depict the tangential velocity, circumferential velocity and normal velocity profiles with increasing magnetic parameter, *M*. *M* defines the relative influence of the Lorentz magnetic body force and the rotational inertial force in the regime. It is a modification of the Stuart magnetic interaction parameter [47]. When *M* = 1 both forces contribute equally. For *M* > 1 the magnetic drag force dominates the rotational inertial force. Since this force acts in the tangential-circumferential plane, these velocity components experience the inhibiting effect i. e. both tangential (*f'*) and circumferential (*g*) velocities are suppressed. However, the Lorentz force does not act in the normal direction (z-axis) since the magnetic field is applied in this direction. The destruction in momentum in the tangential and circumferential directions is re-distributed in the normal direction which manifests in a strong acceleration effect, although the flow direction is reversed (negative values of *f*). For the case *M* = 0 the magnetic effect is negated, and tangential and circumferential velocity magnitudes are maximum. Conversely the normal velocity is minimized for the non-magnetic case. No flow reversal is induced in either the tangential, and circumferential flow fields. The tangential flow always peaks at some distance from the cone surface exhibiting a parabolic profile. With increasing magnetic field, the peak progressively migrates towards the cone surface. The circumferential velocity topology is however a classical monotonic decay from the wall (cone surface) into the free

stream. A more prominent modification in tangential flow is instigated with stronger magnetic field relative to the circumferential (azimuthal) flow. For the normal (axial) flow, a monotonic decay is also observed from the cone surface to the freestream, although the topologies are inverted compared with the circumferential flow. The profiles consistently converge smoothly in the free stream indicating the prescription of an adequately large infinity boundary condition in the MATLAB code. The imposition of an external static magnetic field clearly exerts a significant impact on velocity distributions. This non-intrusive technique therefore afford coating engineers with a powerful mechanism for regulating the flow and in turn manipulating boundary layer thickness and coating homogeneity [4, 487].

Figure 6-8 visualize the evolution in the tangential, circumferential, normal velocities with permeability parameter, K. The Darcian linear porous drag components in the tangential and circumferential momentum Eqns. (9) and (10) i. e. $a_1 f'/K$ *and* $a_1 g/K$, respectively, are inhibiting forces. As K increases, both these forces are reduced and this assists in percolation of the magnetic nanofluid in the porous medium. Tangential velocity is therefore boosted strongly. A weak elevation in circumferential velocity is also computed. Conversely the normal velocity component is suppressed since momentum is drained away from the swirling regime in the normal direction. Careful manipulation of the actual permeability of the porous medium, K^*, which is simulated via K, enables successful modification in all three tangential, circumferential and normal velocity fields. The boundary layer structure can therefore also be adjusted in coating deposition operations in magnetic nanofluids.

Figs. 9-11 display the impact of Richardson number, Ri, on tangential, circumferential and normal velocities. Ri expresses the relative contribution of natural convection to forced convection. Usually natural (free) convection becomes negligible when $Ri < 0.1$, and forced convection is negligible when $Ri > 10$. In the plots shown, Ri is varied from 1 to 4 and therefore both free and forced convection are present. Increasing Ri strongly boosts the tangential velocity, and the peak magnitude is migrated closer to the cone surface. Thermal buoyancy therefore accelerates the tangential flow. However, it has the converse effect on the circumferential flow and produces a weak deceleration effect. A much stronger retarding effect is generated in the normal flow velocity. Ri features in the coupling term, in the tangential momentum eqn. (9), viz, $-a_3/a_2\, Ri\, (\theta)$. It is absent in the circumferential momentum equation (10) and this explains the relatively weak influence on circumferential velocity since the influence is indirect, not direct.

Figure 12 illustrates the variation in the temperature with Dufour number, *Du*. It is seen that as *Du* rises, the temperature also rises and thermal boundary layer thickness is accentuated on the cone surface. Thermal enhancement is generated by the mass concentration gradient associated with the movement of the nanofluid particles. This produces an energy flux in the concentration field which is irreversible. *Du* features in multiple terms in the energy conservation (thermal boundary layer) eqn. (11), for example, $Du\, f'Sc\, \phi$, $Du\, \gamma\, \phi^n$, $fScDu\, \phi'$ which all contribute to the modification in energy distribution (thermal diffusion). With greater values of *Du* there is also a morphing in the temperature profile from inverted parabolic distributions to essentially a linear decay from the cone surface to the free stream. It is important to include this effect in coupled coating transport processes and neglection will lead to erroneous computations of temperature distributions.

Figure 13 illustrates the temperature variation with *Sr*. The Soret or thermo-diffusion effect is the reciprocal phenomenon to the Dufour effect. Both are intimately connected to the molecular diffusivity of species. Soret effect produces a thermal gradient which influences the concentration field. It features again in several terms, but this time in the species diffusion (concentration boundary layer) eqn. (12), viz $a_5 Pr\, f'Sr\, \theta$, $-a_4\, f'Sc\phi$, $a_5 Pr\, f\, Sr\theta'$. As *Sr* is increased this exacerbates molecular diffusion and simultaneously alters the temperature distribution, albeit negatively. As *Sr* rises, the temperature is therefore suppressed, and thermal boundary layer thickness is depleted. Profiles transform from a gradual monotonic decay to a strongly inverted parabolic profile with higher values of *Sr*.

Figure 14 shows the temperature profiles through the boundary layer regime transverse to the rotating cone surface with various chemical reaction strength parameter, γ. An increase in destructive chemical reaction intensity produces a greater quantity of new species. This influences the temperature diffusion via coupling of the concentration eqn. (12) with the temperature equation (11) in the term, $-a_4\, \gamma\phi^n$, *and furthermore explicitly via the term,* $Du\gamma\phi^n$, appearing in the energy eqn. (11). The profiles are morphed from strongly parabolic to gentle monotonic topology with higher values of γ. Concentration boundary layer thickness is also significantly reduced with more intense chemical reaction.

Figure 15 illustrates the temperature profiles with a variation in Schmidt number, *Sc.* As Sc increases, the molecular (species) diffusivity of the reactive nanoparticles is reduced relative to the momentum diffusivity. *Sc* also expresses the ratio of these two diffusion rates. When Sc > 1 momentum diffusion dominates molecular diffusion. However, for *Sc* < 1 molecular

diffusion dominates momentum diffusion. For *Sc* = 1 both diffusion rates are equivalent as are the momentum (hydrodynamic) and species boundary layer thicknesses. The diffusivity decreases considerably with increasing molecular weight, while the viscosity increases. With molecular diffusion exceeding momentum diffusion, as shown in Fig. 14, the heat diffusion is inhibited since the convection transport is coupled. This influences the temperature field adversely and depletes both temperature and thermal boundary layer thickness. In all cases maximum temperature arises at the cone surface and minimum temperature is computed away from the wall in the free stream (edge of the coating boundary layer).

Figures 16 and 17 display the impact of Dufour number and Soret number on concentration. With augmentation in *Du*, the species diffusion is opposed in the regime. This reduces the concentration magnitudes and decreases nanoparticles species boundary layer thickness. Again, there is a sizeable contribution to the modification in temperature distribution due to the nonlinear terms, $Du\, f'Sc\, \phi$, $Du\, \gamma\, \phi^n$, $fScDu\, \phi'$, in eqn. (11). For low values of *Du* the temperature decay is approximately linear from the wall to the free stream. However, increasing curvature is induced in the profiles with greater *Du* values indicating a nonlinear interplay with more intense Dufour effect. Concentration is on the contrary enhanced with increasing Soret number, *Sr*. Temperature gradient (which drives nanoparticles from hotter to colder zones) is therefore assistive to the molecular diffusion of nanoparticles whereas concentration gradient is inhibitive towards heat diffusion. Concentration boundary layer thickness rises under the driving influence of thermal gradient. Again, the primary terms contributing to this behaviour are $a_5 Pr\, f'Sr\, \theta$, $-a_4\, f'Sc\phi$, $a_5 Pr\, f\, Sr\theta'$. *With regard to coating consistency, to optimize* thermal, hydrodynamic and species diffusion behavior, Soret and Dufour effects can be manipulated via the selection of appropriate nanoparticles and also wall temperature conditions to ensure that the deposition rate is high and spatially uniform, and that the coating film has the desired physicochemical properties [47].

Figure 18 reflects the concentration profiles for different Schmidt number, *Sc*. With a rise in *Sc*, the molecular diffusivity of the nanoparticles is depleted relative to the momentum diffusion. Higher *Sc* implies smaller molecular diffusivity. This curtails the motion of nanoparticles *within the swirling boundary layer coating regime* which manifests in a reduction in the concentration (although transport *to the cone surface* will be boosted). Enhanced nanoparticle concentration can therefore be only achieved with lower molecular diffusion rates of the nanoparticles [48]. Concentration boundary layer thickness also exhibits a decrement

with greater Schmidt number. Linear descents in the concentration profiles are computed at all values of Schmidt number.

Figure 19 and 20 plot the response in nanoparticle concentration profiles with an increment in reaction intensity parameter, γ and the order of chemical reaction, n. The nature of the chemical reaction as defined in Eqn. (5) is *homogenous and destructive*. This transforms the original nanoparticle species into a new species and therefore the concentration magnitudes of the original species are significantly reduced. As γ increases the profiles also transition from a curved nature to a linear nature and the concentration (solutal) boundary layer thickness is also depleted. As the order of the chemical reaction morphs from a linear (n =1), through quadratic (n = 2) to cubic (n = 3) and finally quartic (n =4), there is a marked decrease in concentration magnitudes. The key term in eqn. (12) is - $a_4\ \gamma\phi^n$, *which exerts a tangible effect on concentration distribution.* A significant depletion in concentration boundary layer thickness will also arise. The implication is that for conventional models in the coating literature where only first order reactions are studied, concentrations are over-predicted. The significant depletion in concentrations with higher order chemical reaction cannot be captured with such models and as testified to by the plots, is simulated accurately with n >1. The nature of higher order chemical reaction is relevant to other chemical synthesis techniques deployed in nanomaterial coating [47].

Figures 21 and 22 represent the variation in tangential and circumferential skin friction for a rise in *Richardson number, Ri* and *magnetic interaction parameter, M*. As *Ri* rises, thermal buoyancy force is accentuated, and the tangential flow is accelerated which increases the surface skin friction at the cone surface i. e. values become progressively less negative. However, the converse effect is induced in the circumferential skin friction which becomes more negative with increment in Richardson number. Increasing magnetic body force parameter, *M*, considerably boosts the tangential skin friction (linear ascents are plotted) whereas it suppresses strongly the circumferential skin friction (linear decays). *M* features in the Lorentzian body force components, Mf'/a_2 in eqn (9) and Mg/a_2 in eqn. (10). Although both forces are linear, they impart a profound influence on the electrically conducting nanofluid swirling flow. The former is found to accelerate the tangential flow whereas the latter depletes the circumferential flow.

Figures 23 and 24 display the variation in tangential and circumferential skin friction on the rotating cone surface with simultaneous increase in permeability parameter, K, and magnetic

parameter, *M*. As *K* rises, the tangential Darcy body force (porous medium drag force) is modified, and this decelerates the flow. Tangential skin friction is therefore impeded. However, the converse pattern is produced in the circumferential skin friction which is found to be increased (values are progressively less negative) with greater permeability parameter and this is once again attributable to the re-distribution in momentum in the swirling regime. Again, the tangential skin friction grows with higher values of magnetic parameter whereas the circumferential skin friction is depleted. A combination of magnetic field, permeability and Richardson number (thermal buoyancy) can therefore be achieved where desired characteristics in either tangential or circumferential (azimuthal) flow fields is required during coating deposition.

Figures 25 and 26 depict the evolution in local Nusselt number (local rate of heat transfer at the cone surface) and local Sherwood number (local rate of mass transfer at the wall) with a simultaneous increment in *Schmidt number, Sc*, and *magnetic interaction parameter, M*. When *Sc* rises, the suppression in molecular diffusivity results in local heat transfer rate being considerably accentuated indicating that greater heat flux to the cone surface is achieved from the boundary layer regime. The relative influence of thermal convection to thermal conduction (which is also expressed by Nusselt number) will also be boosted. Conversely there is a decrement in the local mass transfer values with greater Schmidt number.

Tables 3-5 present the variation in *skin friction components i.e. $f''(0)$, $g'(0)$, Nusselt number, $-\theta'(0)$ and Sherwood number, $-\phi'(0)$* with a change in *γ, Du, Sr and n* respectively. For a particular value of *n*, an elevation in chemical reaction rate parameter (γ) reduces both tangential and circumferential skin friction values and Nusselt number but increases the Sherwood number (**Table 3**). An increase in the order of chemical reaction (*n*) consistently increases tangential and circumferential skin friction values, Nusselt number and Sherwood number. Overall compared to low order chemical reactions (n =1), high order chemical reactions (n = 2,3,4) produce considerable elevation in heat and mass transfer rates to the revolving cone surface which is beneficial in achieving more consistent coatings during spin manufacture operations. **Table 4** shows that with increasing Dufour number, both tangential and circumferential skin friction are suppressed, as is local Nusselt number whereas the local Sherwood number (wall mass transfer rate) is enhanced. Finally with increasing Soret number, **Table 5** shows that a similar effect is induced in all wall transport characteristics as with increasing Dufour number, at any value of the order of chemical reaction, *n*.

5. CONCLUSIONS

Inspired by emerging technologies in rotating magnetic nanofluid coatings, a theoretical and computational study of chemically reactive Cu−H_2O magnetohydrodynamic (MHD) nanofluid swirl coating boundary layer flow, heat and mass transfer from a revolving vertical electrically insulated cone adjacent to a porous medium under a radial static magnetic field, has been presented. Dufour and Soret cross diffusion effects and thermal and solutal buoyancy forces have been included. To simulate chemical reaction of the diffusing species encountered in manufacturing processes, a higher order chemical reaction formulation is also featured. Via suitable scaling transformations, the governing nonlinear coupled partial differential conservation equations and associated boundary conditions have been transformed to a nonlinear ordinary differential boundary value problem. MATLAB-based shooting quadrature with a Runge-Kutta method has been employed to solve the emerging system. Verification of the accuracy of the MATLAB solutions has been achieved with existing literature. The present analysis has shown that:

(i) Compared to low order chemical reactions, high order chemical reactions achieve greater rates of heat and mass transfer at the cone surface.

(ii) Tangential velocity and circumferential velocity are reduced with increment in magnetic parameter whereas normal velocity is enhanced.

(iii) Tangential velocity and circumferential velocity are enhanced with greater values of permeability parameter whereas normal velocity is depleted.

(iv) Tangential velocity is boosted with Richardson number (thermal buoyancy effect) whereas both circumferential velocity and normal velocity are decreased.

(v) Temperature and thermal boundary layer thickness are enhanced with increment in Dufour (diffuso-thermal) number and chemical reaction rate parameter whereas they are reduced with increasing Soret (thermo-diffusion) and Schmidt numbers.

(vi) Increasing Soret number elevates the concentration magnitudes (and species boundary layer thickness) whereas the opposite trend is observed with increasing Dufour number, chemical reaction rate parameter and Schmidt number.

(vii) A rise in chemical reaction rate enhances the local Sherwood number whereas it suppresses the local Nusselt number and both tangential and circumferential skin friction components at the cone surface.

(viii) An increment in Dufour number and Soret number elevates local Sherwood number but depletes the local Nusselt number and both skin friction components.

The present simulations have identified some intriguing phenomena in spin coating with copper-water magnetic nanofluids. Attention has however been confined to Newtonian behaviour. Future studies may explore rheological behaviour [44] with a range of models and also address wall slip effects [49] and alternative magnetic nanoparticles e. g. silver, zinc [46] etc. These will be communicated imminently.

CONFLICT OF INTEREST STATEMENT

The authors declare that they have no conflict of interest.

REFERENCES

[1] F. Klocke *et al*., Surface integrity in electrochemical machining processes: An analysis on material modifications occurring during electrochemical machining, *Proceedings of the Institution of Mechanical Engineers, Part B: Journal of Engineering Manufacture*, 232 (4) (2017). doi.org/10.1177/09544054177034

[2] PT Pajak et al., Process energy analysis for aluminium alloy and stainless steel in laser-assisted jet electrochemical machining, *Proceedings of the Institution of Mechanical Engineers, Part B: Journal of Engineering Manufacture,* 220, 3, (2006). doi.org/10.1243/095440505X3271

[3] K. Xiao *et al.*, Selective patterned growth of single-crystal Ag–TCNQ nanowires for devices by vapor–solid chemical reaction, *Advanced Functional Materials*, 18, 3043-3048 (2008).

[4] DeLongchamp, Dean M., Brandon M. Vogel, Youngsuk Jung, Marc C. Gurau, Curt A. Richter, Oleg A. Kirillov, Jan Obrzut *et al*. "Variations in semiconducting polymer microstructure and hole mobility with spin-coating speed." *Chemistry of materials* 17, 5610-5612 (2005).

[5] M.A. Uddin *et al*., Thermal and chemical stability of a spin-coated epoxy adhesive for the fabrication of a polymer optical waveguide, *Chem. Mater.*, 16, 23, 4806–4811 (2004).

[6] Rahman, M., Al-Lawatia, M.: Effects of higher order chemical reaction on micropolar fluid flow on a power law permeable stretched sheet with variable concentration in a porous medium. *The Canadian Journal of Chemical Engineering* 88(1), 23–32 (2010).

[7] Palani, S., Kumar, B.R., Kameswaran, P.K.: Unsteady MHD flow of an UCM fluid over a stretching surface with higher order chemical reaction. *Ain Shams Engineering Journal* 7(1), 399–408 (2016).

[8] Sastry, R.: Melting and radiation effects on mixed convection boundary layer viscous flow over a vertical plate in presence of homogeneous higher order chemical reaction. *Frontiers in Heat and Mass Transfer (FHMT)* 11 (2018).

[9] Choi, S.U.S., Eastman, J.: Enhancing thermal conductivity of fluids with nanoparticles. *Proceedings of the ASME International Mechanical Engineering Congress and Exposition, San Francisco, USA*, 66 (1995).

[10] Jessica Vidales-Herrera and Israel López, Chapter 3 - Nanomaterials in coatings: an industrial point of view, In *Handbook of Nanomaterials for Manufacturing Applications, Micro and Nano Technologies*, 51-77 (2020).

[11] Buongiorno, J.: Convective transport in nanofluids. *ASME J. Heat Transfer* 128(3), 240–250 (2005).

[12] Tiwari, R.K., Das, M.K.: Heat transfer augmentation in a two-sided lid-driven differentially heated square cavity utilizing nanofluids. *International J. Heat Mass Transfer* 50(9-10), 2002–2018 (2007).

[13] J.J. Reinosa *et al.* Copper Based Hydrophobic Ceramic Nanocoating, *J. European Ceramic Society* 32(2):277–282 (2012).

[14] K.M. Hyie *et al.,* The physical and magnetic properties of electrodeposited Co-Fe nanocoating with different deposition times, *J. Nanomaterials*, Volume 2013 | Article ID 680491 | https://doi.org/10.1155/2013/680491 (2013).

[15] M. Shamshuddin, S.R. Mishra, O. Anwar Bég and Ali Kadir, Adomian computation of radiative-convective stretching flow of a magnetic non-Newtonian fluid in a porous medium with homogeneous–heterogeneous reactions, *Int. J Modern Physics B,* 33 (2) (2020). (28 pages).

[16] Swain, K., Parida, S.K., Dash, G.C.: Higher order chemical reaction on MHD nanofluid flow with slip boundary conditions: A numerical approach. *Mathematical Modelling of Engineering Problems* 6(2), 293–299 (2019).

[17] Eid, M.R., Mabood, F., Mahny, K.L.: On 3D Prandtl nanofluid flow with higher-order chemical reaction. *Proceedings of the Institution of Mechanical Engineers, Part C: Journal of Mechanical Engineering Science* 235(19), 3962–3974 (2021).

[18] P.K. Pattnaik, S. R. Mishra, O. Anwar Bég, Umar F. Khan and J.C. Umavathi, Axisymmetric radiative titanium dioxide magnetic nanofluid flow on a stretching cylinder with homogeneous/heterogeneous reactions in Darcy-Forchheimer porous media: *intelligent nanocoating simulation, Materials Science and Engineering B* (2021). doi.org/10.1016/j.mseb.2021.115589 (26 pages)

[19] S.O. Solawu, M. Shamshuddin, O. Anwar Bég, Influence of magnetization, variable viscosity and thermal conductivity on Von Karman swirling flow of H_2O-Fe_3O_4 and H_2O-Mn-$ZNFe_2O_4$ ferromagnetic nanofluids from a stretchable rotating disk: smart spin coating simulation, *Materials Science and Engineering B,* 279 (2022) 115659 (13 pages).

[20] A.F.S. Afshar *et al*., Mass transfer at rotating cone electrodes, *Journal of Applied Electrochemistry*, 21, 32–39 (1991).

[21] Kenyon, K.E. Cone rotating in a fluid. *Natural Science,* 12, 1-3 (2020).

[22] C. Y. Wang, Boundary Layers on rotating cones, discs and axi-symmetric surfaces with a concentrated heat source, *Acta Mechanica,* 81, 245-251 (1990).

[23] C. L. Tien and D. T. Campbell, Heat and mass transfer from rotating cones, *J. Fluid Mechanics,* 17, 105-112 (1963).

[24] Roy, S., Takhar, H.S., Nath, G.: Unsteady MHD flow on a rotating cone in a rotating fluid. *Meccanica* 39(3), 271–283 (2004).

[25] O. Anwar Bég, V. R. Prasad, B. Vasu and R.S.R. Gorla, Computational modelling of magnetohydrodynamic convection from a rotating cone in orthotropic Darcian porous media, *J. Braz. Society Mech Sci Eng,* 39, 2035–2054 (2017).

[26] S.E. Ahmed *et al.,* MHD Ellis nanofluids flow around rotating cone in the presence of motile oxytactic microorganisms, *International Communications in Heat and Mass Transfer* 134, 106056 (2022).

[27] F. T. Zohra, M.J. Uddin and A.I. Ismail, O. Anwar Bég and A. Kadir, Boundary layer anisotropic slip magneto-bioconvection flow from a rotating cone to a nanofluid with Stefan blowing effects, *Chinese J. Physics,* 56, 432-448 (2018).

[28] Puneet Rana, R. Bhargava and O. Anwar Bég, Finite element simulation of unsteady MHD transport phenomena on a stretching sheet in a rotating nanofluid, *Proc. IMECHE- Part N; J. Nanoengineering and Nanosystems,* 227, 77-99 (2013).

[29] G.A. Moatimid *et al.,* A Casson nanofluid flow within the conical gap between rotating surfaces of a cone and a horizontal disc, *Scientific Reports*, 12, Article number: 11275 (2022).

[30] Abdal, S.; Siddique, I.; Abualnaja, K.M.; Afzal, S.; Jaradat, M.M.M.; Mustafa, Z.; Ali, H.M. On time dependent rheology of Sutterby nanofluid transport across a rotating cone with anisotropic slip constraints and bioconvection. *Nanomaterials,* 12, 2902 (2022). doi.org/10.3390/ nano12172902.

[31] Jagadha, S., Gopal, D., Kishan, N.: Nanofluid flow of higher order radiative chemical reaction with effects of melting and viscous dissipation. *Journal of Physics: Conference Series*, vol. 1451 (2020).

[32] Alaidrous, A.A., Eid, M.R.: 3-D electromagnetic radiative non-Newtonian nanofluid flow with Joule heating and higher-order reactions in porous materials. *Scientific Reports* 10(1), 1–19 (2020).

[33] Gopal, D., Saleem, S., Jagadha, S., Ahmad, F., Almatroud, A.O., Kishan, N.: Numerical analysis of higher order chemical reaction on electrically MHD nanofluid under influence of viscous dissipation. *Alexandria Engineering Journal* 60(1), 1861–1871 (2021).

[34] Rajani, D., Hemalatha, K.: Effects of higher order chemical reactions and slip boundary conditions on nanofluid flow. *Int. J. of Eng. Res. and Application* 7(5), 36–45 (2017).

[35] M.M. Bhatti, C.M. Khalique, Tasveer Bég, O. Anwar Bég and Ali Kadir, Numerical study of slip and radiative effects on magnetic Fe_3O_4-water-based nanofluid flow from a nonlinear stretching sheet in porous media with Soret and Dufour diffusion, *Modern Physics Letters B* 33, 2050026 (24 pages) (2020).

[36] C. Sulochana *et al*., Numerical investigation of magnetohydrodynamic (MHD) radiative flow over a rotating cone in the presence of Soret and chemical reaction, *Propulsion and Power Research*, 7, 91-101 (2018).

[37] I. Siddique *et al.*, Soret and Dufour effects on unsteady MHD second grade nanofluid flow across an exponentially stretching surface, *Scientific Reports*, 12, Article number, 11811 (2022).

[38] Dankovich, T.A., Smith, J.A.: Incorporation of copper nanoparticles into paper for point-of-use water purification. *Water Research*, 63, 245–251 (2014).

[39] MD. Shamshuddin, S.R. Mishra, O. Anwar Bég, T.A. Bég and Ali Kadir, Computation of radiative Marangoni (thermocapillary) magnetohydrodynamic convection in Cu-water based nanofluid flow from a disk in porous media: smart coating simulation, *Heat Transfer* (2020). DOI: 10.1002/htj.21963 (20 pages).

[40] I. Foffa *et al.,* A Copper nanoparticles-based polymeric spray coating: Nanoshield against Sars-Cov-2, *Journal of Applied Biomaterials & Functional Materials (2022).* https://doi.org/10.1177/228080002210763

[41] Ingle AP, Duran N, Rai M. Bioactivity, mechanism of action, and cytotoxicity of copper-based nanoparticles: a review. *Appl Microbiol Biotechnol*., 98: 1001–1009 (2014).

[42] Verma, K., Borgohain, D., Sharma, B.: Soret and Dufour effects on MHD flow about a rotating vertical cone in presence of radiation. *J. Math. Comput. Sci*. 11(3), 3188–3204 (2021).

[43] Sebdani, S.M., Mahmoodi, M., Hashemi, S.M.: Effect of nanofluid variable properties on mixed convection in a square cavity. *International Journal of Thermal Sciences* 52, 112–126 (2012).

[44] J. C. Umavathi, K. Vajravelu, O. Anwar Bég and Umar F. Khan, Unsteady squeezing flow of a magnetized dissipative non-Newtonian nanofluid with radiative heat transfer and Fourier-type boundary conditions: numerical study, *Archive of Applied Mechanics (2022).* (17 pages) https://doi.org/10.1007/s00419-022-02211-4

[45] J. C. Umavathi and O. Anwar Bég, Computation of thermo-solutal convection with Soret-Dufour cross diffusion in a vertical duct containing carbon/metallic nanofluids, *Proc. IMechE Part C- J. Mechanical Engineering (2022).* DOI: 10.1177/09544062211072693 (17 pages).

[46] J.C. Umavathi and O. Anwar Bég, Augmentation of heat transfer via nanofluids in duct flows using Fourier-type conditions: theoretical and numerical study, *Proc. IMeche Part E- J. Process Mechanical Engineering (2021).* DOI: 10.1177/09544089211052025 (16 pages)

[47] Gaur S, Khanna AS. Functional coatings by incorporating nanoparticles. *Nano Res Appl.* 1(1):1-8 (2015).

[48] Pilotek S, Tabellion F. Nanoparticles in coatings: tailoring properties to applications. *Eur. Coat. J.,* 4:170-80 (2005).

[49] O. Anwar Bég, Noman Kabir, Uddin M.J, Ahmad Izani Md. Ismail, Yasser AlginahI, Numerical investigation of Von Karman swirling bioconvective nanofluid transport from a rotating disk in a porous medium with Stefan blowing and anisotropic slip effects, *Proc. IMechE- Part C- J. Mechanical Engineering Science* (2020). DOI: 10.1177/0954406220973061 (19 pages)